University of Bergen
Faculty of Mathematics and Natural Sciences
Department of Physics and Technology

Master of Science Thesis

Characterization of Scintillation Crystals for Positron Emission Tomography

by

Jostein Sæterstøl

Supervisor: Assoc Prof Eli Renate Grüner
Co-supervisor: Prof Dieter Röhrich

Bergen, June 2010

Summary

The main purpose of this thesis has been to characterize BGO and LYSO crystals of different sizes with respect to decay time and energy resolution. BGO crystals have been used as a reference material. The work presented here is part of a research project initiated by the Department of Physics and Technology, University of Bergen, and the Department of Radiology, Haukeland University Hospital. The project is entitled "Improved diagnostics in Positron Emission Tomography (PET) through the extraction of temporal characteristics from detector system and tissue." The main objective of the project is to use temporal information to improve sensitivity and specificity in imaging with PET technology.

For the BGO crystals, a decay time of 305 ± 6 ns has been found. The energy resolution measured with the use of the best optical grease was $16.6 \pm 0.1\%$.

Ten small (2x2x16 mm^3) LYSO crystals have been found to have a decay time of 47.0 ± 0.3 ns. The best obtained energy resolution for these crystals is $13.3 \pm 0.2\%$.

The larger crystals generally show a somewhat longer decay time. The 5x5x20 mm^3 crystals show decay times of 48.0 to 48.5 ns. Of the crystal sizes tested, the 5x5x20 mm^3 crystals show the best energy resolution. With the use of optical grease, an energy resolution of $11.4 \pm 0.1\%$ has been measured.

The linearity of the energy spectra has been investigated by the use of two different radioactive sources with a total of three different energy peaks. The linearity is very good both for the BGO and LYSO crystals.

A qualitative investigation of the interaction efficiency of LYSO crystals of different sizes has been performed. The number of counts in the photopeak is compared to the total number of counts in the spectrum.

No apparent difference is found increasing crystal length. The thickness of the crystal influences the interaction efficiency greatly.

In addition to the characterization of different crystals, an introductory experiment concerning the rate of single, random, and true counts as a function of the activity has been performed in the PET scanner at the PET centre at Haukeland University Hospital (HUH).

Acknowledgements

I would like to thank all the people who have helped and encouraged me during my work on this thesis. I could never have done this on my own. I would especially like to thank:

My main supervisor Assoc. Prof. Renate Grüner, for introducing me to the field of medical physics, and for all the help and support I have received during my work on this project. You are an eager, supportive, and encouraging supervisor, guiding me through this work in a very good way.

My co-supervisor Prof. Dieter Röhrich, for his ideas, and for sharing of his wide knowledge on the field of radiation detectors.

Njål Brekke, for all the help you've given me with the equipment and the software in the lab, and for the enlightening discussions. Also, Dominik Fehlker, for the practical help you have offered me during this last year. Thank you to the people in our office and in the lab for the time spent together these last couple of years.

The people at the PET centre at Haukeland University Hospital that have spent time making the experiment with the PET scanner possible. Thank you for being interested in making the scanner available, and for your interest in my experiment.

My mother, my father, and my two sisters for always believing in me and encouraging me.

My wife and friend Trine for all your support, encouragement and patience, and for always believing in me. You are great.

Finally, my daughter, Hanna Oline: you melt my heart.

Bergen, June 30th 2010

Jostein Sæterstøl

Contents

List of Abbreviations

Abbreviation	Description
ADC	Analog-to-Digital Converter
APD	Avalanche Photodiode
CNR	Contrast to Noise Ratio
CT	Computed Tomography
LAAPD	Large Area Avalanche Photodiode
MPPC	MultiPixel Photon Counter
NEC	Noise Equivalent Count Rate
PET	Positron Emission Tomography
PMT	Photomultiplier Tube
SNR	Signal to Noise Ratio
SPECT	Single Photon Emission Computed Tomography
TDC	Time-to-Digital Converter
TOF	Time of Flight

List of Crystal Materials

Crystals	
BaF_2	Barium Fluoride
BGO	Bismuth Germanate
CsF	Cesium Fluoride
GSO	Gadolinium Oxyorthosilicate
$LaBr_3$	Lanthanum Bromide
LSO	Lutetium Orthosilicate
LYSO	Lutetium Yttrium Orthosilicate
NaI(Tl)	Sodium Iodine doped with Tallium

List of Figures

List of Tables

Chapter 1

Introduction

The first chapter will deal with the theoretical basis for this thesis. This includes ionizing radiation and its interaction with matter, positron emission tomography (PET) and its basic physics, and lastly the physics of the detectors used in PET. The introductory experiment on a clinical PET scanner will also be presented.

1.1 Radioactivity and Ionizing Radiation

Radioactivity refers to the spontaneous emission of radiation from atomic nuclei. The radiation comes from the radioactive decay of the nuclei. For a large number of nuclei, the decay process can be described as

$$N = N_0 e^{-\lambda t} \tag{1.1}$$

where N_0 is the number of nuclei at time $t = 0$, N is the number of nuclei at time t, and λ is the decay constant of the radioisotope.

The activity, or decay rate, A, of the radioactive decay is found as

$$A = \left| \frac{\mathrm{d}N(t)}{\mathrm{d}t} \right| = \lambda N = \lambda N_0 e^{-\lambda t} \tag{1.2}$$

The half-life of a radioactive isotope, $T_{1/2}$, is defined as the time it takes until half of the nuclei of an isotope have disintegrated. Equation (1.3) shows the relation between the half-life and the decay constant.

$$N = \frac{N_0}{2} = N_0 e^{-\lambda T_{1/2}} \Rightarrow T_{1/2} = \frac{\ln 2}{\lambda} \tag{1.3}$$

The type of radiation resulting from a decay depends on the decay mode. The main decay modes are α-, β- and γ-decay. The PET technique is based on the radioactive decay of β^+-emitters. These are proton rich isotopes which enter a more stable energy state by converting a proton into a neutron following the transformation

$$p \rightarrow n + e^+ + \nu \tag{1.4}$$

where p is a proton, n is a neutron, ν is an electron neutrino and e^+ is a positron. The positron and the electron neutrino share the energy that is released during the decay and carry it away as kinetic energy and mass. The energy of the positron will therefore be continuously distributed up to the maximum energy, as shown in Figure 1.1. For PET, the useful outcome of this decay is the β^+-particle; the positron. This will be explained further in Section 1.3.1

Neutron rich isotopes often decay through β^--decay. A neutron is spontaneously transformed into a proton

$$n \rightarrow p + e^- + \overline{\nu} \tag{1.5}$$

The electron and the antineutrino share the excess energy of the reaction. The electron typically has a range of 1 mm in lead [1]. The range is dependent on the electron energy.

The α-decay is mostly common in atoms with a high atomic number, Z. The α-particle is a ^{4}He nucleus which is emitted at discrete energies

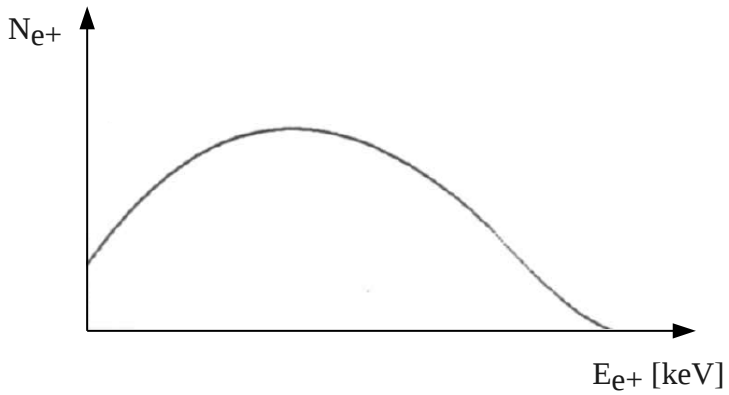

Figure 1.1: Energy distribution of the positrons following a β^+-decay. Because of the simultaneously emitted neutrino, the energy of the positrons is distributed continuously up to a maximum energy. The maximum energy is dependent on the radioactive isotope involved. Figure reproduced from Ref. [2]

depending on the isotope. α-particles are considered heavy, and have a very short range, typically 0.02 mm in lead [1]. Equation (1.6) describes the transformation that happens during an α-decay.

$$ {}^{\mathrm{A}}_{\mathrm{Z}}\mathrm{X} \rightarrow {}^{\mathrm{A}-4}_{\mathrm{Z}-2}\mathrm{Y} + {}^{4}_{2}\mathrm{He} \tag{1.6} $$

Here, A is the mass number and Z is the atomic number of the atom. X and Y denotes the atomic element.

After a radioactive decay, the daughter nucleus is often left in an excited state. To enter ground state, a γ-decay often occurs. The gamma photon carries away the extra energy as kinetic energy. For the work presented here, the detection of gamma photons is the important subject. The interaction of gamma photons with matter will therefore be treated in more detail.

1.2 Ionizing Photons in Matter

Ionizing particles, such as α- and β-particles, are slowed down by continual collisions with electrons and nuclei in the matter they traverse. This way, their energy is transferred to the matter. Photons interact differently with matter than particles do. A photon may travel a long distance without interacting with the matter. When it interacts, it is said to interact catastrophically [3]. Instead of continual collisions, it loses large fractions of its energy through one or a few interactions. A mono-energetic ray of gamma photons with initial intensity, I_0, traveling through matter is attenuated along its path. At the distance, x, into the matter, a fraction of the photons will have been stopped. The intensity has then been reduced to I as described by Equation (1.7)

$$ I = I_0 e^{-\mu x} \tag{1.7} $$

where μ is the attenuation coefficient. The attenuation coefficient depends both on the density and the effective atomic number of the matter, and on the energy of the incident photon.

A photon interacts through different mechanisms depending on its energy, and the density and effective atomic number of the matter it traverses. For PET applications, where the photons have an initial energy of 511 keV, the two main interaction mechanisms are the photoelectric effect and Compton scattering.

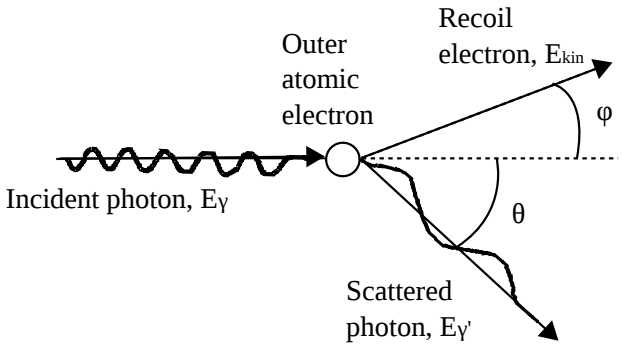

Figure 1.2: Illustration of Compton scattering. The incident photon is deflected an angle, θ, transferring some of its energy to the recoil electron. Illustration reproduced from Ref. [3]

1.2.1 The Photoelectric Effect

The photoelectric effect involves a photon interacting with an orbital electron and transferring all its energy to the electron. The electron is ejected from the atom, and deposits its energy locally through interactions with the surrounding matter. The atom is left excited and re-enters a stable state in one of two ways [3]. The so-called Auger effect involves using the excess energy to free an Auger electron from the atom. Alternatively, a characteristic X-ray is emitted, carrying away the excess energy. This is called fluorescence.

1.2.2 Compton Scattering

Compton scattering is illustrated in Figure 1.2. A Compton scattered photon transfers a fraction of its energy to the recoil electron it interacts with. The amount of energy transferred to the electron is dependent on the scattering angle of the photon. The photon's energy after the interaction can be calculated as [3]

$$E_{\gamma'} = \frac{E_\gamma}{1 + (E_\gamma / m_e c^2)(1 - \cos\theta)} \tag{1.8}$$

where E_γ and $E_{\gamma'}$ is the energy of the photon before and after the scattering, $m_e c^2$ is the electron rest mass energy and θ is the scattering angle of the photon. Compton scattering is the key mechanism for blurring in medical imaging modalities that utilizes ionizing radiation.

1.2.3 Other Interaction Mechanisms

Rayleigh Scattering

Rayleigh scattering is an interaction mechanism with very little energy transfer compared to the previously discussed interaction mechanisms. It is an elastic process, where the photon is deflected, but there is no excitation of the atom it collides with. Rayleigh scattering is more probable for low photon energies in materials with a high atomic number.

Pair Production

During pair production, a photon is converted to a an electron–positron pair. Since the rest energy of each of the created particles is 511 keV, the photon needs an energy of at least 1 022 keV for this process to happen. Because of this, pair production is not relevant to PET applications.

1.3 Positron Emission Tomography

Positron emission tomography (PET) is the most advanced nuclear medicine imaging modality available. Although the technique has been available for some decades, its popularity increased tremendously at the beginning of this century when the combined PET/CT (Computed tomography) scanners became commercially available. These scanners allowed superpositioning of high contrast biochemical PET images on high resolution anatomical CT images.

According to Valk et al. [4], one of the first images of a man using what now is known as PET technology was produced in 1957. Nevertheless, PET is still, maybe more than ever, in rapid development. Research is done to improve sensitivity, spatial resolution, time resolution, signal to noise ratio (SNR), contrast to noise ratio (CNR), and more [4, 5].

1.3.1 The Basic Physics of PET

To perform a PET scan, a radioactive tracer is injected into the patients body. The tracer is a positron emitter which decays according to Equation (1.4). The positron is emitted from the tracer with a kinetic energy up to an isotope specific maximum energy. This kinetic energy is subsequently deposited in the surrounding tissue, primarily through inelastic collisions with atomic electrons [4]. When all the kinetic energy is lost,

the positron annihilates with an electron. This produces two photons. Each photon has an energy of 511 keV, corresponding to the rest energy of the electron and the positron. The photons are emitted back-to-back to conserve momentum and are in turn detected in the PET detector system.

Two photons from one annihilation will reach the detectors nearly simultaneously, i.e. within a few nanoseconds. Therefore, the PET detectors are operated in coincidence mode. In coincidence mode a time window with a predefined duration 2τ is used. If two photons are detected within this time window the detection is counted as an event. Each event is assigned a line of response, which is a straight line between the two detector modules that detected the photons. If both photons were measured to have an energy within a predefined energy window, and the line of response is within a valid acceptance angle, the event is counted as valid [4]. The lines of response from the valid events are used for image reconstruction.

Even though two photons are detected as coincident and the event is counted as valid, the assigned line of response need not pass through the actual point of annihilation. This will be the case if one or both of the photons have undergone interactions, i.e. lost energy or changed direction, in the tissue before they are detected. The coincidence detections can be divided into different categories. The three main categories [4] are listed below:

True coincidence is when both photons pass through the tissue without interacting with it, and subsequently are detected. A true line of response is assigned to the event.

Scattered coincidence arises if one or both of the photons are Compton scattered before detection.

Random coincidence involves two photons from different annihilations detected within one time window.

These three coincidence detection possibilities are illustrated in Figure 1.3. In addition, it is possible that only one photon, or more than two photons, are detected within one time window. This is known as single events and multiple events, respectively. Single events are discarded since no line of response can be determined. Multiple events are discarded since there is no way to determine which photons come from the same annihilation point. Scattered and random coincidences reduce the

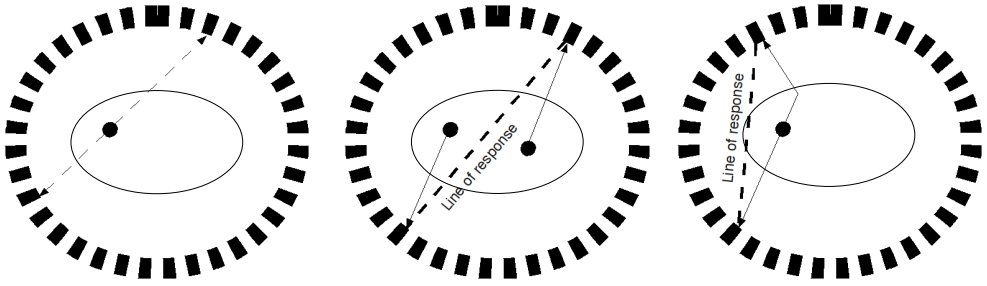

Figure 1.3: Three different kinds of coincidence detection: true, random, and scattered coincidence. The ring of black rectangles illustrates the detector ring. The oval object illustrates the patient body. The black dots are the points of annihilation. Only the true coincidence gives a true line of response. The others contribute to noise in the final reconstructed image.

contrast and increases the noise in the final reconstructed image [4] and are thus unwanted.

Since Compton scattered photons loose some of their initial energy in the scattering, it is possible to exclude them from the data by applying an energy threshold to the measurement. Photons with energy below the threshold will then be disregarded. For this method to be efficient, the energy resolution of the detector system needs to be very good. This is not the case with common PET scanners using BGO as scintillator material in the detectors. The energy threshold for these scanners may need to be kept as low as 350 keV in order to preserve all the true events [6]. According to Equation (1.8), a photon must be scattered more than 55 degrees to lose that much energy in a single Compton scattering. This is shown in Figure 1.4, where the photon's scattering angle is plotted as a function of its final energy. Also shown is the energy resolution a detector needs to have to be able to distinguish this photon from an unscattered photon. The plot is a visualization of Equation (1.8). Even with a detector energy resolution of 5%, a photon can be scattered near 20 degrees before the detector is able to distinguish it from an unscattered photon. Other techniques are therefore required for scatter correction. These include multiple energy window methods, empirical methods and simulation based methods [4] that will not be discussed in this thesis.

The number of random coincidences increases with both increased ac-

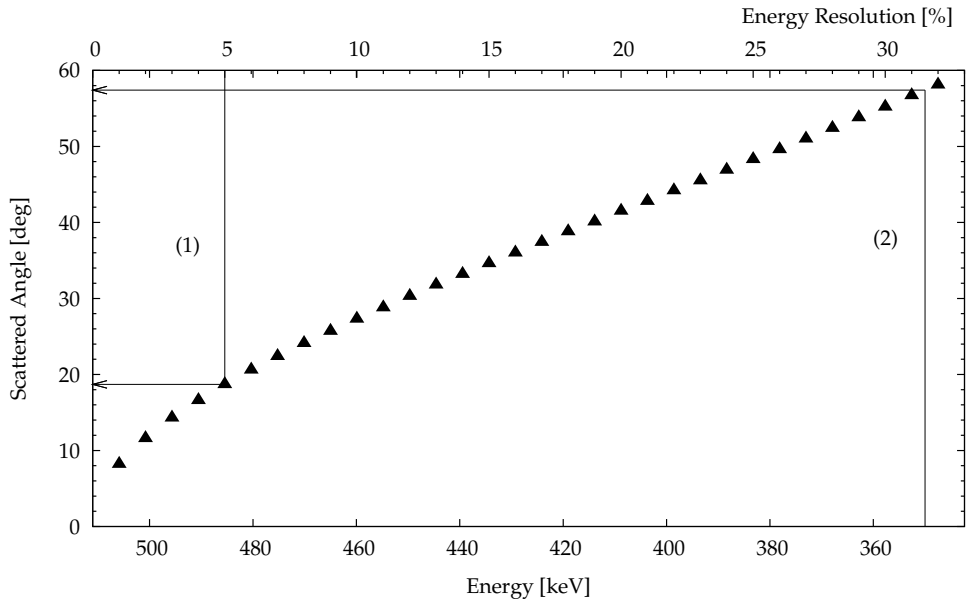

Figure 1.4: The scattered angle, θ, a Compton scattered photon is deflected as a function of how much energy it loses in the scattering. Also shown is the energy resolution a detector needs to have to be able to distinguish the scattered photon from an unscattered one. Arrow (1) shows the minimum angle a scattered photon must be deflected for a detector system with 5% energy resolution to be able to distinguish it from an unscattered one. Arrow (2) shows this for typical PET scanners based on BGO with an energy threshold of 350 keV.

tivity, and increased length of the time window. The random coincidence count rate for two detectors a and b is given by [4]:

$$R_{ab} = 2\tau N_a N_b \tag{1.9}$$

where 2τ is the width of the time window and N is the single event rate for detector a and b, respectively. The random rate can thus be reduced by reducing the width of the time window. It can also be reduced by estimating its contribution based on Equation (1.9) or by using a delayed time window to model it [4].

1.3.2 Fundamental Limitations in PET

PET images are reconstructed based on the lines of response information. The lines of response are in turn calculated based on the points of annihilation. Because positrons have a certain range in the tissue before annihilation occurs, the point of annihilation does not reflect precisely

the point of the decay, which is the real point of interest. Fluorine-18 (^{18}F) is the most used tracer isotope in PET [7]. The positron emitted from ^{18}F has a maximum kinetic energy of 0.633 MeV and a mean range in water of 0.6 mm [4].

Furthermore, the photons resulting from the annihilation are not emitted strictly back-to-back if the positron or the electron annihilating still has a kinetic energy larger than zero at the time of annihilation. This is known as non-collinearity. The fraction of non-collinear photons has been estimated to be as high as 65% in water [4].

The finite range of the positron and the non-collinearity of the annihilation photons lead to a fundamental lower limit of the spatial resolution for PET instrumentation. The value of this limit has been investigated by several research groups, concluding that for a human whole-body PET scanner with a detector ring diameter of 80 cm the limit is $\sim$2 mm with ^{18}F used as radiotracer [8–10]. Yet, typical spatial resolution in clinical PET images today is about 4 mm.

1.3.3 Time of Flight PET

Light travels about 30 cm/ns in air. This means that if an annihilation point is situated 15 cm from the center of a line of response, the two photons from this annihilation will arrive at the detectors with a time difference Δt of about 1 ns. This time difference is not measured in conventional PET. In time of flight (TOF) PET this time difference is measured and utilized to determine more accurately the point of annihilation. The annihilation point is calculated according to

$$\Delta s = c\Delta t/2 \tag{1.10}$$

where Δs is the distance from the center of the line of response to the annihilation point, Δt is the time difference of the photon arrivals, and c is the speed of light. The smallest Δt a scanner can measure is known as the scanner's coincidence time resolution. The TOF principle is illustrated in Figure 1.5. The upper part illustrates conventional PET, whereas the bottom part illustrates TOF PET.

The idea of TOF PET is not a new one; the first TOF PET scanners were introduced in the 1980's. At this time, BGO was the leading scintillator material in PET due to its very high stopping power for 511 keV photons [11, 12]. For time of flight measurements, faster scintillators were needed. However, the available faster scintillators at that time, such as CsF and

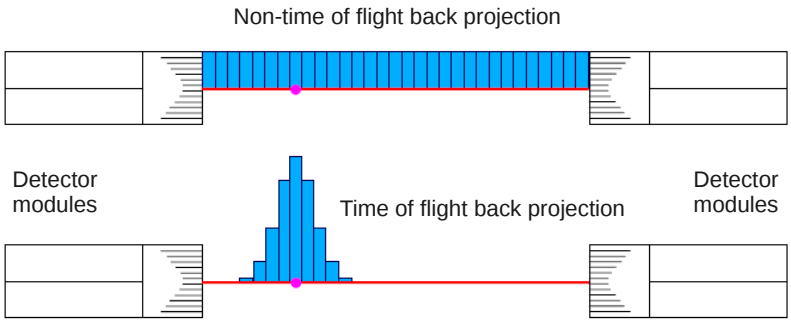

Figure 1.5: Difference between conventional PET and TOF PET. At the top, conventional PET is illustrated. At the bottom, the increased accuracy in determining the annihilation site using time of flight information is shown. The line between the two detector modules is the line of response, while the dot on the line is the actual point of annihilation. The bars illustrate the calculated probability that the annihilation occurred within that area.

BaF_2, suffered from poor stopping power and too low light output, resulting in an overall image quality being poorer for the TOF PET scanners than for conventional PET scanners [11, 13]. The development of TOF PET was therefore mostly abandoned by the early 1990's [14]. Later, new scintillator materials such as LSO and LYSO have been developed. These materials combine high stopping power with good timing properties, enabling a fresh approach to the idea of using TOF technology in PET. In 2005/2006, Philips introduced the first commercial PET scanner with time of flight capabilities. The scanner is built using LYSO scintillator crystals. It has a coincidence time resolution of about 600 ps [15].

The time of flight information reduces the noise propagation along the line of response during reconstruction of images [11, 16, 17]. For analytical reconstruction methods, the gain in SNR has been modeled as [11, 16]

$$\text{SNR}_{\text{TOF}} = \sqrt{\frac{D}{\Delta x}} \cdot \text{SNR}_{\text{non-TOF}} \tag{1.11}$$

where D is the patient diameter and Δx is the localization uncertainty. This approximation, although based on simple assumptions, gives a useful idea of the gain from TOF technology for different time resolutions and patient sizes. The noise equivalent count rate (NEC) is a measure of a scanners effective sensitivity. It is defined as

$$\text{NEC} = \frac{T^2}{T + S + R} \tag{1.12}$$

Table 1.1: The gain in NEC using TOF PET for different time resolutions and patient diameters. The gain higher for larger patient diameters and better time resolutions.

Δt [ps]	Δx [cm]	TOF NEC Gain (10 cm diameter)	TOF NEC Gain (40 cm diameter)
100	1.5	6.7	26.7
300	4.5	2.2	8.9
500	7.5	1.3	5.3
1000	15.0	0.7	2.7

where T, S and R is the number of true, scattered and random coincidences, respectively. The NEC and SNR are related as NEC = SNR^2. Table 1.1 gives an overview of the sensitivity gain calculated from these formulas.

1.4 Performance Evaluation of a Clinical PET System

In order to investigate the rate of single events, random coincidences, and true coincidences in a clinical PET scanner as a function of the activity, an in vitro experiment was set up at the local PET centre, Department of Radiology, Haukeland University Hospital (HUH). The PET scanner at HUH is a Siemens Biograph PET-CT. The scanner estimates the number of single events, random coincidences, and true coincidences real time during a scan.

The experiment was prepared by filling five syringes, each with approximately 80 MBq of radioactive ^{18}F. The exact activity was measured for each of the syringes. By knowing the initial activity at a certain point of time, the activity at any time can be calculated. The five syringes were put inside the scanner, and a scan was started. After one minute, one of the syringes was removed from the scanner. This was repeated every one minute until there were no syringes left. The scanner's values for the single, random, and true rate were read every two seconds during the whole scan. The rate of single events, random coincidences, and true coincidences was plotted as a function of the activity inside the scanner.

The results from the measurements on the clinical PET scanner are shown in Figure 1.6. The true rate is considerably higher than the random

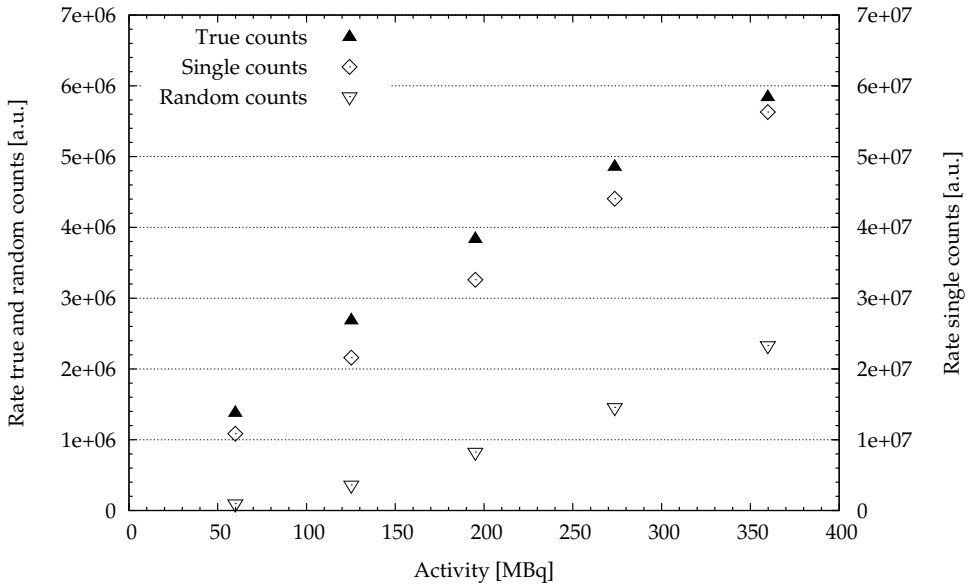

Figure 1.6: Rate of singles, randoms and trues in a clinical PET scanner as a function of activity. Note that the plot of the single counts has a separate y-axis. The single rate is one order of magnitude higher than the true rate. The results are from data measured on the clinical PET scanner at HUH.

rate for all the measured activities. The slope of the true rate seems to be decreasing slightly with increasing activity. The slope of the random rate is increasing with increasing activity. It is likely that at even higher activities the random rate will increase beyond the true rate. The rate of single counts is about a factor ten higher than the true rate.

Although these measurements are not done according to any standard, such as the NEMA NU 2-2007 standards, and as such are not directly comparable to other published data, a brief comparison of the results with those obtained by Schmitz et al. [18] is interesting. The current measurements show a lower random rate, relative to the true rate, compared to that obtained in Ref. [18]. The most likely explanation for this might be the different crystals involved. The scanner at HUH is built using LSO crystals, while Schmitz et al. [18] is investigating a BGO scanner. The faster LSO crystals allow for a shorter coincidence time window, which in turn reduces the random rate (see Equation (1.9)). The main focus of this thesis is to investigate the basic properties of such crystals (BGO and LYSO).

1.5 Scintillator Crystals

PET scanners utilize scintillation detectors. These detectors consist of a scintillator crystal coupled to a photodetector. The scintillation crystal converts the gamma radiation into visible light, which is converted to an electrical signal and amplified by the photodetector.

There exists both organic and inorganic scintillator materials. Organic scintillators are plastics made of aromatic hydrocarbons, while inorganic scintillators are made of alkali halides or oxides [3]. Organic scintillator materials are not used in PET scanners due to their very low stopping power for gamma radiation and low light output [19, 20]. They will not be discussed further in this thesis.

1.5.1 The Scintillation Process

Inorganic crystals that emit light when exposed to ionizing radiation are called luminescent. On an atomic level, pure inorganic scintillator crystals show a repeating pattern, known as a crystal lattice. A crystal's luminescence is a property of its crystal lattice. The lattice determines discrete energy bands available for the electrons in the material. These energy bands are illustrated in Figure 1.7. The conduction band represents electrons that are free to migrate through the crystal. Below the conduction band is a forbidden region, followed by the valence band. The valence band represents the outer-shell electrons [20]. In a semiconductor, the forbidden region, E_g, between the valence band and the conduction band is in the order of a few electronvolts (eV) [19].

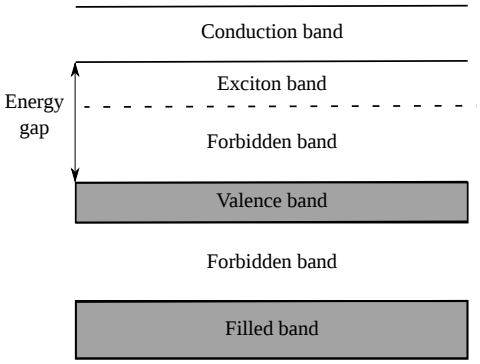

Figure 1.7: Energy bands in an ideal insulating crystal

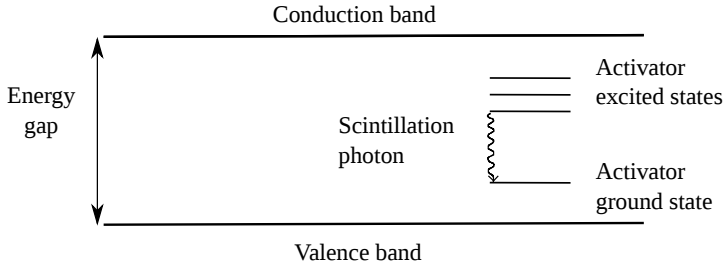

Figure 1.8: Energy band structure of an activated crystalline scintillator. The activator creates allowed energy levels within the previously forbidden region. Electrons de-exciting from these energy levels can cause emission of scintillation photons. Figure reproduced according to Ref. [20]

A gamma photon absorbed in a scintillator knocks loose a fast electron, which in turn produces a cascade of secondary electrons [21]. The secondary electrons cause electrons to be elevated from the valence band into the conduction band. Positive holes are left in the valence band, so that electron-hole pairs are created. An elevated electron may return to the valence band by the emission of a photon. In a pure crystal, this is an inefficient process [20]. A pure crystal also has a large band gap, E_g, resulting in few electron-hole pairs created per unit of energy deposited. To increase the efficiency of the electron-hole creation, small amounts of impurities are purposely added to the crystal. The impurities, or activators, create luminescence centers in the forbidden energy region. Electrons can de-excite through these centers, and photons with energy corresponding to visible light is emitted [20]. This is illustrated in Figure 1.8.

1.5.2 Properties of Scintillator Crystals

Different scintillator crystals have different properties. The choice of a scintillator material for a specific application is a trade-off between different important parameters. Some important properties are described below. Table 1.2 gives an overview of different properties for some relevant crystals.

Table 1.2: Properties of some scintillator crystals. Different papers present somewhat different values, but they are mainly in concordance. Data taken from Ref. [11] unless otherwise noted.

Crystal	Density [g / cm^3]	Decay time [ns]	Total light output [photons / MeV]	Energy resolution at 662 keV [%]
BGO[a]	7.1	300	6 000	10.2[b]/ 20[c]
LYSO(Ce)	7.1	41	32 000	–[*]
LSO(Ce)	7.4	40	32 000	10.0[b]
$LaBr_3$(Ce)	5.1	16	63 000	2.9[d]
NaI(Tl)[a]	3.7	230	38 000	6.6[a]
BaF_2	4.9	0.8	12 000	11.4[a]

[a] Data taken from Ref. [4]. [b] Data taken from Ref. [22].
[c] Data taken from Ref. [23]. [d] Data taken from Ref. [12]. [*] Similar to LSO.

Decay Time

The decay time is a measure of how fast a crystal emits the light after the absorption of a gamma photon. Many crystal materials show decay pulse shapes that are single- or multi-exponential. For a single-exponential pulse, the decay time is defined as the time it takes for the pulse amplitude to decrease to the fraction $1/e$ of its maximum amplitude value. The decay time influences the timing properties of the crystal. Shorter decay time increases the count-rate capability of the detector [3, 24]. It also implies a shorter rise time, which decreases trigger jitter, so that the time resolution of the detector system can be improved. This is important to increase the benefit of TOF PET.

Energy Resolution

The energy resolution of a detector system indicates how well it is able to distinguish the energy of gamma photons with similar energies. The intrinsic energy resolution of the scintillator materials often dominates the achievable energy resolution of a detector system. When a pulse height spectrum (energy spectrum) is obtained, the energy resolution, R, is defined as the full width at half maximum (E_{FWHM}) of the energy peak in

question. It is often expressed as a percentage of the energy corresponding to the position of the peak along the x-axis, E_0:

$$R = \frac{E_{\text{FWHM}}}{E_0} \cdot 100\% \tag{1.13}$$

When the energy peak contains a sufficient number of counts, it is often Gaussian shaped [3]. The relationship between the energy resolution and the standard deviation, σ, of the peak can then be expressed as

$$E_{\text{FWHM}} = 2.35 \cdot \sigma \tag{1.14}$$

Improved energy resolution improves the signal-to-noise ratio of the reconstructed images [13] and reduces the influence of the random coincidences [12].

The primary limitation on the energy resolution of a scintillator crystal is the number of photons detected by the photodetector [25]. This number is subject to Poisson distribution. A higher number of photons gives a lower relative uncertainty, and therefore a better energy resolution. For a given crystal with a known light output, the Poisson distribution results in a theoretical limit on the best energy resolution obtainable. The light output of a scintillator crystal is explained below.

Many scintillator crystals, including LYSO, show a poorer energy resolution than would be expected when considering counting statistics [26]. The explanation is the fact that the number of light photons produced per unit of deposited energy is dependent on the energy of the particle exciting the crystal [26, 27]. This is known as non-proportionality in the light output. When a gamma photon excites the crystal via e.g. photoelectric effect, it knocks loose an electron. This electron also excites the crystal, and knocks loose more electrons. The cascade of electrons resulting all have different energies, but the total sum of energies equals the incident energy of the gamma photon [26]. The scintillation light is produced by a number of electrons with varying energies. If the crystal has a proportional light output, the same amount of scintillation light will be produced each time the same amount of energy is deposited in the crystal. This is because the total energy of all the electrons sums up to the energy deposited by the incident gamma photon. If, however, the crystal has a non-proportional light output, the amount of scintillation light will vary from even when the deposited energy is the same, because the cascade of electrons is different each time. This will cause a degradation of the energy resolution.

In a scintillation detector, the energy resolution of the whole system, R, is often divided into three parts: the intrinsic energy resolution of the crystal, R_i, the transfer resolution, R_p, and the resolution of the photomultiplier tube (PMT), R_M [28]. Equation (1.15) shows how the different factors contribute to the overall energy resolution.

$$R^2 = R_i^2 + R_p^2 + R_M^2 \tag{1.15}$$

The transfer resolution is often assumed to be negligible compared to the two other factors [29]. The photomultiplier resolution is described by

$$R_M = 2.35\sqrt{\frac{1 + v(M)}{\overline{N}\overline{p}}} \tag{1.16}$$

where $v(M)$ is the variance in the photomultiplier gain and $\overline{N}\overline{p}$ is the number of photoelectrons. More detailed, $\overline{N}$ is the mean number of photons created by a gamma photon in the scintillation crystal. $\overline{p}$ is the average transfer efficiency, i.e. it represents the probability that a scintillation photon in the crystal actually causes a photoelectron to be multiplied by the PMT.

Stopping Power

The stopping power, or stopping efficiency, of a scintillator crystal indicates if the crystal is an efficient absorber of the incoming gamma photons. The stopping power depends on the crystals density and its effective atomic number (Z_{eff}) [23, 24]. A dense crystal which also has a high effective atomic number has a high stopping power. A high stopping power is important to absorb as much as possible of the incoming radiation. Table 1.3 shows the attenuation length, fraction of photoelectric events and interaction fraction for 511 keV photons in different scintillator crystals. The interaction fraction is calculated as

$$P(x) = e^{-x/\lambda} \tag{1.17}$$

where $P(x)$ is the probability that a photon has not interacted after traveling a distance x in a crystal with attenuation length λ. The interaction fraction is calculated as $1 - P(x)$.

Light Output

The light output, or light yield, is a measure of how much light a crystal emits per unit of energy deposited in it. This is often measured as the

Table 1.3: Attenuation length and interaction probabilities for 511 keV photons in different crystals. Attenuation length and photoelectric fraction is taken from Ref. [12]. The interaction fraction is calculated by Equation (1.17).

Crystal	Attenuation length at 511 keV [mm]	Photoelectric fraction [%]	Interacting fraction in crystal [%]	
			20 mm	30 mm
BGO	10.4	40	85	94
LSO	11.4	32	83	93
$LaBr_3$	21.3	13	61	76

number of emitted light photons per MeV of deposited energy. A high light output is important in PET applications to improve accuracy, spatial resolution and energy resolution [24], since more light gives a more well-defined light pulse [23].

Other Factors

Other factors are also important to consider when choosing scintillator material for a particular application. These include matching of the wavelength spectrum of the light photons from the crystal with the sensitive range of the photodetector, the refractive index of the crystal, its ruggedness, whether it is hygroscopic or not, and its price [21, 24].

The combination of high light output and short decay time is not very common in scintillator crystals [24]. When LSO was discovered as a scintillator material, it appeared to have combined some of the best properties from two of the most used crystal materials at the time, NaI(Tl) and BGO [3, 4, 30]. NaI(Tl) has a high light output but suffers from poor stopping power due to the low density and effective atomic number. BGO exhibits good stopping power but a low light output. Both NaI(Tl) and BGO are still widely used in a range of applications. NaI(Tl) has dominated the scintillator material market for more than 50 years [21] and is still the material of choice in SPECT applications. The extensive use of BGO crystals for PET scanners shows that stopping power has been the most crucial property for this applications [23].

1.5.3 BGO Crystals

Bismuth germanate (BGO) is a very dense scintillator material (7.1 g/cm^3) with an effective atomic number of 73 [31]. Despite its poor light output and long decay time, this has made it the crystal of choice in PET scanners for 20 years. BGO is most often quoted with a decay time of 300 ns. Its scintillation pulse shape is actually bi-exponential. A small component with a decay time of 60 ns is also present in the pulse shape [32]. The small component contains about 10% of the total number of scintillation photons [20]. The small amount of scintillation photons in this component outrules its interest for PET applications, since even the main pulse of the BGO crystals contains very few scintillation photons compared to alternative crystals. The total light output of BGO crystals is about 12 000 photons per MeV. The energy resolution obtainable with BGO crystals is some places reported to be about 10%, while others state about 20% (see Table 1.2).

1.5.4 LSO and LYSO Crystals

LSO is an acronym for Lutetium Orthosilicate, (Lu_2SiO_5: Ce), while LYSO is an acronym for Lutetium Yttrium Orthosilicate ($Lu_{(2-x)}Y_xSiO_5$: Ce). The Ce-part shows that these crystals are doped or activated with cerium. The two crystals mostly have similar properties. The main difference is the fact that the yttrium component in LYSO makes it easier and cheaper to grow [33].

LSO has a density of 7.4 g/cm^3 and an effective atomic number, $Z_{e\,ff}$, of 65 [31]. The density and effective atomic number of LYSO depends on the amount of yttrium present. LYSO is often quoted with a density similar to that of LSO. Pepin et al. [31] have investigated LYSO with the chemical formula $Lu_{0.6}Y_{1.4}SiO_5$:Ce. With such a large amount of yttrium, the properties are considerably different than for LSO. The density is reduced to 5.37 g/cm^3, and Z_{eff} to 54.

The literature value of the decay times of LSO and LYSO crystals is about 40 ns. Some vendors give a value of 50 ns for the decay time, and Ludziejewski et al. [34] have reported 47 ns for LSO crystals. Large amounts of yttrium may alter the decay time of LYSO considerably [31].

The energy resolution of LSO/LYSO crystals is typically around 10%, but may vary within a large range for different samples [33]. With small crystals, energy resolutions of 7.5% and 7.9% have been reported [12, 20].

The energy resolution of the LSO/LYSO crystals suffers because of non-proportionality in the light output as described above.

The total light output reported ranges from about 25 000 to 32 000 photons per MeV [4, 35]. Some of the variations in the reported values for different properties of LSO/LYSO crystals are due to the improvements made in crystal growth processes [31].

The LSO/LYSO crystals are themselves radioactive due to the Lu-176 isotope [4]. Lu-176 is a β-emitter primarily decaying to an excited state of Hf-176. This isotope emits gamma photons with energies of 307 keV, 202 keV, and 88 keV. The crystals self-emission causes the crystal to be excited and produce scintillation light. This results in a self-count of 39 cps/g (counts per second per gram) (see Appendix A).

1.5.5 Other Crystal Materials

Both NaI(Tl) and GSO(Ce) have been used in commercial PET scanners. NaI(Tl) shows a very good light output, but suffers from poor stopping power. GSO has a reasonably good stopping power and better intrinsic energy resolution properties than LSO. However, it is a fragile crystal material and must be handled with care [23].

The list of scintillator crystals relevant for PET applications is growing. $LaBr_3$(Ce) is one of the new materials showing promising properties: high light output, short decay time, and excellent intrinsic energy resolution [36]. The main drawback of this crystal is its relatively low density of 5.1 g/cm^3. It is also hygroscopic, which means it is degraded by being exposed to humidity. It must therefore be sealed in a box by the producer.

1.6 Photodetectors

Scintillation light from the scintillator crystals needs to be amplified and turned into an electrical signal for further processing. In PET, and many other applications, a photomultiplier tube (PMT) is used for this purpose. However, advancing semiconductor technology now makes it possible to use solid state detectors for the same purpose.

To ensure that as much as possible of the scintillation light is detected by the photodetector, optical grease can be used to couple the crystal and the photodetector. This way, the gap of air between the two is substituted with a medium with a refractive index matching the refractive indices of the crystal and the window of the photodetector better. Less light will

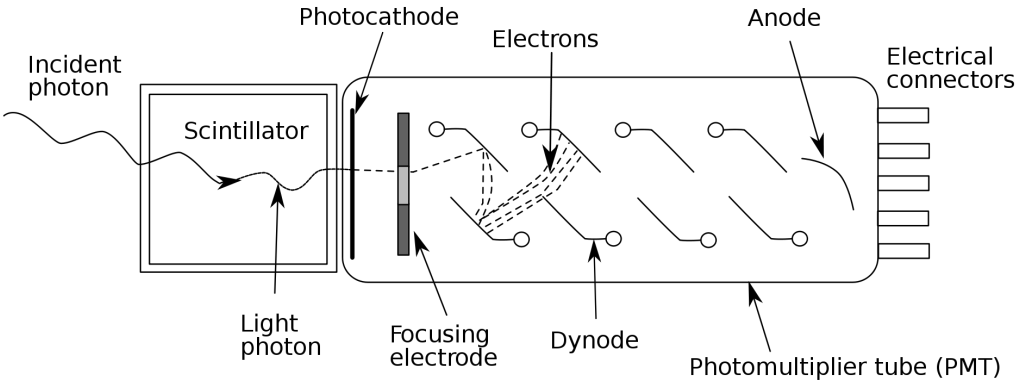

Figure 1.9: Schematic overview of a PMT. The scintillation photons hit the photocathode and a photoelectron may result. The photoelectron is accelerated by the electric field, and multiplied at each dynode throughout the PMT.

be reflected and more light will be transmitted to the photodetector. The crystal may also be covered with a diffuse or reflective material so that the light will not escape the crystal on the sides not coupled to the photodetector.

1.6.1 Photomultiplier Tubes

A PMT is a vacuumed tube consisting of a photocathode, focusing electrodes, several dynodes and an anode (see Figure 1.9). High voltage, typically 1 000 to 2 000 volts [37], is applied across the tube so that each dynode is at a higher potential than the previous one.

The light incident on the PMT hits the photocathode. The energy absorbed from a light photon is transferred to an electron within the photoemissive material. The electron might migrate to the surface of the material and escape into the vacuum of the tube [20]. It is then called a photoelectron. A PMTs quantum efficiency describes the probability of photoelectron emission when a photon hits the photoemissive material. The quantum efficiency of a typical PMT is about 20% to 30% [4, 20] but PMTs with quantum efficiencies of 40% are available [38].

The electric field within the tube accelerates the photoelectrons. The focusing electrodes guide the photoelectron to the first dynode. In the dynode, the absorbed energy of the photoelectron causes re-emission of several secondary electrons. The secondary electrons are then in turn accelerated towards the second dynode, where more electrons are struck

loose. A typical PMT consists of 10 to 12 dynodes [4] and amplifies the signal with a factor 10^5 to 10^7 [39]. This factor is known as the gain of the tube.

PMTs are known to exhibit linear amplification of the signal, high gain, good SNR, and a short signal pulse [20]. The technology is well-known and very reliable. On the downside, PMTs are quite large and have a relatively low quantum efficiency [4]. They are also sensitive to magnetic fields, which limits their usefulness in magnetic environments.

1.6.2 Semiconductor Detectors

Although the PMT has been the photodetector of choice for many applications for decades, recent advances in semiconductor detector technology have made these detectors a real alternative to the PMT for a number of applications [20]. Among their advantages over PMTs are a higher quantum efficiency, more compact size, lower power consumption, and a lower price. Unlike PMTs, semiconductor detectors are insensitive to magnetic fields.

Semiconductor Materials and the Photodiode

In semiconductor materials, the outer shell electrons are organized in energy bands, as illustrated for the scintillator crystals in Figure 1.7. For a pure semiconductor, the forbidden energy band is of such a size that thermal excitation of electrons from the valence band into the conduction band is possible. Such an excitation leaves a positively charged hole in the valence band. In a pure semiconductor, the number of electrons and holes is equal.

By adding impurity atoms (doping) to the material, discrete energy levels can be created within the forbidden region. The original balance of electrons and holes is shifted so that there are more electrons than holes, or more holes than electrons. The former results in an n-type semiconductor, and the latter results in a p-type semiconductor.

For the n-type semiconductor, discrete energy levels are created near the conduction band. From here, the excess electrons can easily be elevated into the conduction band, making them free to move. The p-type semiconductor contains discrete energy levels slightly above the valence band. Electrons from the valence band are easily excited here, leaving extra holes behind.

A photodiode consists of an n-type and a p-type semiconductor in close contact. The holes from the p-side will start to drift towards the the n-side, and the electrons from the n-side will drift towards the p-side because of the difference in charge concentration. This will cause an electric potential to be established. A depletion region is created in the middle, containing no charged particles. A charged particle entering the depletion region is swept away by the electric field. By applying a reverse bias voltage, the electric potential is increased. The increased electric field causes any charged particle entering the region to be swept away more quickly.

Photons entering the depletion region excites electrons from the valence band into the conduction band. Positively charged holes are left in the valence band. The applied electric field causes the electrons and holes to drift towards the n-side and the p-side, respectively. Thus, a current flows through the diode.

An avalanche photodiodes (APDs) is a photodiode with operating voltage above a certain limit. In an APD, the excited electrons and holes gain enough energy from the electric field to produce secondary electron-hole pairs, which in turn are accelerated by the electric field. The process is repeated for the new electron-hole pair, and an avalanche of electrons and holes is created. The result is that the signal from an APD is amplified significantly compared to the signal from a conventional photodiode.

If the bias voltage is increased above the *breakdown voltage* of the APD, the number of electron-hole pairs will only continue to grow. This is referred to as operating the avalanche photodiode in Geiger mode. To stop the avalanche, a quenching circuit is used [40].

Multipixel Photon Counters

Multipixel photon counters (MPPCs) is Hamamatsu's name for their pixelated avalanche photodiodes. Each pixel in an MPPC is an avalanche photodiode operated in Geiger mode. The output signal from the MPPC is proportional to the number of pixels that has been fired, and therefore the number of photons that has been detected.

1.7 Motivation

The work presented here is part of a research project in cooperation between the Department of Physics and Technology, University of Bergen, and the Department of Radiology, Haukeland University Hospital. The project is entitled "Improved diagnostics in Positron Emission Tomography (PET) through the extraction of temporal characteristics from detector system and tissue." The main objective of the project is to use temporal information to improve sensitivity and specificity in imaging with PET technology.

As part of this project, detailed knowledge and understanding of all parts of the detector system is needed. Previously, different Geiger mode avalanche photodiodes have been characterized with respect to absolute gain, dark rate and more [41]. Although thorough work has been published regarding the decay time and energy resolution of scintillator crystals, the need to understand the basics of this initiated the work presented here. The properties of two crystal types are investigated. For improved PET imaging it is important that the crystals have a short decay time, high energy resolution, are linear with respect to energy of incoming photons, and have only small variations between geometrically identical crystals. Furthermore it is important to see how crystal geometry influences the measurements, e.g. through evaluation of interaction efficiency. There was also a need to gain first-hand experience by working with the crystals, and setting up a test-bench for measuring their properties in order to be able to fulfill the goals of the overall project.

Chapter 2

Materials and Methods

Two different types of scintillator crystals, BGO and LYSO, have been characterized with respect to decay time and energy resolution. BGO has been the work horse in PET applications for more than two decades, while LYSO has recently been introduced in commercial scanners. This chapter will present the equipment used, the experimental setups, and the methods used to characterize the crystals. Decay time and energy resolution have been measured simultaneously. The setup for this will therefore mainly be described in one section, Section 2.2.

2.1 Laboratory Equipment

All measurements have been carried out in a custom-made black box to ensure a dark environment. The box is equipped with connectors on two sides used to supply the detectors with power and to read out the detector signals. The signals from the detectors are sampled by an analog-to-digital-converter (ADC)[1]. The ADC is placed in a VME crate. The signal from the ADC is fed into a computer via a VME–PCI bridge. The software package LabView from National Instruments, USA, has been used for data acquisition. Data analysis and some plotting has been performed using the data analysis framework ROOT [42], while most basic plotting has been done using gnuplot [43]. Relevant product sheets for the different equipment used, are appended.

[1] CAEN 4 Ch, 14 bit, 2 Gs/s ADC, model V1729A. Dynamical Range: -1 V to 1 V

2.1.1 Black Box

The black box is made of aluminium and is painted with black paint on all inner surfaces. Ideally, the box would be totally lightproof. This is not the case. Two black blankets have been used to cover the box on the outside, so that less light will be able to enter the box. Light leakage is especially crucial to the measurement of decay time because these measurements involve measuring single-photons, as will be described in Section 2.2. The method used to measure leakage light will be described in Section 2.2.5, when the experimental setup has been presented.

2.1.2 Teflon Tape

To obtain good results, it is important to detect as much of the scintillation light as possible. The scintillator crystal sends scintillation light in all directions. To direct the light towards the photodetector, the crystal is wrapped in teflon tape[2] on all sides except the one coupled to the detector. Teflon tape is a diffuse reflector. The angle a photon is reflected is independent of its incident angle. Since scintillation photons are reflected at arbitrary angles back into the crystal, the teflon tape increases the amount of photons that reach the detector.

2.1.3 Optical Grease

Two different types of optical grease have been tested: BC-630 silicon optical grease obtained from Saint-Gobain Crystals and Optical Gel Code 0608 from Cargille Laboratories Inc. A small amount of grease is applied to the crystal, and the crystal is pressed onto the photodetector window so that a thin layer of grease couples the crystal to the photodetector.

2.1.4 Scintillator Crystals

This work has characterized BGO and LYSO crystals. The crystals available during the project are listed in Table 2.1 with their code names and sizes. All crystals with code starting with SS have been bought from ScintiStone Technology, LLC. The B and the L is for BGO and LYSO, respectively. The first number is the crystal's size, while the second is its length. The producer of the crystals with code starting with GE is unknown.

[2]PTFE Thread Seal Tape

Table 2.1: All crystals used in the experiments. All crystals have been obtained from ScintiStone Technology, LLC, except the ones marked GE. Their producer is unknown.

Crystal Code	Size [mm^3]	Crystal Code	Size [mm^3]
	BGO		
SSB-5-20-1	5x5x20	SSB-5-20-6	5x5x20
SSB-5-20-2	5x5x20	SSB-5-20-7	5x5x20
SSB-5-20-3	5x5x20	SSB-5-20-8	5x5x20
SSB-5-20-4	5x5x20	SSB-5-20-9	5x5x20
SSB-5-20-5	5x5x20	SSB-5-20-10	5x5x20
	LYSO		
SSL-5-20-1	5x5x20		
SSL-5-20-2	5x5x20		
SSL-5-30-1	5x5x30	SSL-7-30-1	7x7x30
SSL-5-30-2	5x5x30	SSL-7-30-2	7x7x30
SSL-5-40-1	5x5x40	SSL-7-40-1	7x7x40
SSL-5-40-2	5x5x40	SSL-7-40-2	7x7x40
GE-5-20-1	5x5x20	GE-10-20-1	10x10x20
GE-5-20-2	5x5x20	GE-10-20-2	10x10x20
SSL-2-16-1	2x2x16	SSL-2-16-6	2x2x16
SSL-2-16-2	2x2x16	SSL-2-16-7	2x2x16
SSL-2-16-3	2x2x16	SSL-2-16-8	2x2x16
SSL-2-16-4	2x2x16	SSL-2-16-9	2x2x16
SSL-2-16-5	2x2x16	SSL-2-16-10	2x2x16

The density of the LYSO crystals stated by the producer is 7.3 g/cm^3. A selection of the crystals has been weighed to check the density. The scale used has an uncertainty of ± 0.1 g. The volume has been calculated based on the sizes stated by the producer. The uncertainty in the sizes is given as 0.1 mm for all crystal sides.

2.1.5 Photodetectors

The PMTs available in the lab are of type H6780-02 produced by Hamamatsu. Each of them are packed as modules with an internal high-voltage circuit. Therefore, only a low-voltage external power supply is needed in order to use them. During all measurements, the PMTs have been supplied with a bias voltage of 15.00 V and a gain adjust voltage of 0.80 V.

Only one MPPC has been used in the current measurements. This is a Hamamatsu S10362-33-050C MPPC. It was used with a bias voltage of 71.1 V.

2.1.6 Radioactive Sources

The gamma photons detected in PET have an energy of 511 keV resulting from the annihilation. ^{137}Cs is often used in experiments for PET applications since it emits gamma photons with an energy of 662 keV, which is close enough to 511 keV for the results to be comparable. A ^{137}Cs source with an activity of approximately 170 kBq has been used in these experiments.

A ^{22}Na source is also available. This source decays by β^+-decay, and therefore emits photons of 511 keV from the annihilation of the positron with an electron. It also emits gamma photons of 1275 keV. The activity of the source is about 13 kBq. The physical shape of the ^{22}Na source in the lab makes it difficult to place properly next to the crystals. Therefore, the ^{137}Cs source has been used for all the main measurements. The ^{22}Na source has been used to perform measurements to check the linearity of the energy spectrum (see Section 2.3.6).

2.2 Measurement of Decay Time

2.2.1 Method Overview

The setup used for measuring the decay time of the scintillator crystals is shown in Figure 2.1. The setup is based on a method known as the Delayed Coincidence Method presented by Bollinger and Thomas [44]. The method is used to measure the average pulse shape of the scintillation pulse from the scintillator crystal. This is obtained by detecting scintillation light pulses in one PMT and the arrival of single scintillation photons from the same scintillation pulse in another. The arrival time of the single

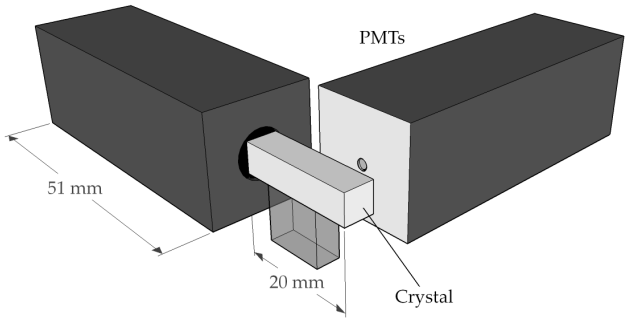

Figure 2.1: Sketch of the setup for measuring decay time of a scintillator. The left PMT is the triggering-PMT, while the right PMT is the measuring PMT.

scintillation photons can then be compared with the time of the detection of the scintillation pulse. This is done for a large number of scintillation pulses. A histogram with the number of single photons versus the difference in arrival times can be plotted and analyzed. The histogram represents the average scintillation pulse of the scintillator crystal. One of the advantages of this method is that it measures the difference between photon arrival times instead of the pulse shape from the PMT. This way, one can determine the real photon pulse shape of the scintillator, without having the signal shape being distorted due to the signal shaping effects of the PMT.

2.2.2 Experimental Setup

Two PMTs are used. One PMT is optically coupled to the scintillation crystal to detect the scintillation light pulse. This PMT is for triggering, and is referred to as the triggering-PMT. The second PMT, referred to as the measuring-PMT, is placed beside the scintillation crystal (to the right in Figure 2.1). The number of photons that reach the measuring-PMT must be reduced so that the arrival time of *single* photons can be determined. The window of the measuring-PMT is therefore covered by a sheet of aluminium foil with a small ($\varnothing \sim 1$ mm) hole in it.

When a scintillation light pulse is created following the absorption of a gamma photon in the scintillator crystal, the light pulse is detected by the triggering-PMT. The measuring-PMT only detects one or a few single photons from each scintillation light pulse. In the original setup

described in Ref. [44], the photon detection efficiency of the PMT was reduced so that the average number of photons detected per triggered light pulse was less than 0.5. This was done because the apparatus was only capable of counting one photon per pulse [45]. If several photons from one pulse reached the measuring-PMT, only the first one would be counted. This would cause an unwanted bias effect since the earlier occurring photons would more likely be measured. The read-out system used in the current measurements is capable of counting several single-photons per light pulse. This is utilized to reduce data acquisition time compared to the original method. A similar approach is described by Moses [45], using a modern time-to-digital converter (TDC).

When a signal is received from the triggering-PMT, a constant fraction triggering is applied. A constant fraction triggering means that the maximum height of the signal pulse is measured, and the trigger is applied when the signal height is some fraction (i.e. 0.2) of its maximum. The fraction is kept constant for all measured signals. The time of the trigger is used as a zero-time reference. The arrival time of single-photons in the measuring-PMT is also recorded. This way, the time between the excitation of the scintillation crystal and the arrival of single scintillation photons from the resulting light pulse can be measured and a histogram can be plotted. An exponential fit can be performed on the histogram to calculate the decay time of the light pulse.

2.2.3 Calculation of Decay Time

The outcome of the decay time measurements is a histogram representing the average shape of the light pulse from the scintillator. The pulse from many scintillators follows an single- or multiexponential decay. The decay time of the scintillation pulse is defined as the time it takes for the pulse to decrease to the fraction $1/e$ of its maximum amplitude value. To calculate this, an exponential fit is performed on the pulse. This is done using the fitting options in ROOT.

The calculated decay time depends on the choice of starting and ending point for the exponential fit. For the BGO crystals, the fitting was started at 100 ns because of the biexponential nature of the scintillation pulse. The fitting was ended at 600 ns. The decay time of the fast scintillation pulse component has not been found due to its insignificance in PET applications. For the LYSO crystals, the starting point has been chosen as the histogram bin with the maximum number of entries. As an end point

for the fitting, 160 ns has been used. Other factors influencing the decay time will also be presented in the following sections.

2.2.4 Determination of Uncertainties

Several factors contribute to uncertainty in the measurements of decay time. Different values of the decay time will be found because of

- Differences in crystals
- Different wrapping in teflon tape
- Different placement of the crystals
- Statistics

To get an overview of the influence of the different factors, several measurements were made.

The influence of statistics was measured by measuring a large continuous data set with one crystal. This data set with 2 million data points was then split into ten data sets, each with 200 000 data points. The decay time was calculated for each of these data sets. The average decay time and the standard deviation, σ_{stat}, of the results were calculated. The resulting standard deviation is the most fundamental factor of uncertainty in these measurements.

The influence of the placement of the crystals was investigated by doing ten measurements on the same crystal, removing and replacing the crystal between each measurement. The average decay time and the standard deviation was calculated. The resulting standard deviation, σ_{tot}, contains both the statistical uncertainty, σ_{stat}, and an uncertainty due to repositioning of the crystal, σ_{repos}. The standard deviation due to the repositioning alone can be calculated by Equation (2.1)

$$\sigma_{\text{tot}}^2 = \sigma_{\text{stat}}^2 + \sigma_{\text{repos}}^2 \tag{2.1}$$

This procedure was only done for one of the BGO crystals (SSB-5-20-5) and two of the LYSO crystals (SSL-5-20-1 and SSL-2-16-2). It has been assumed that the result for the BGO crystal is transferable to the other BGO crystals. It has also been assumed that the result for the 2x2x16 mm^3 crystal is transferable to the other crystals of the same size. Finally, it has been assumed that the result for the 5x5x20 mm^3 LYSO crystal is transferable to the rest of the LYSO crystals.

2.2.5 Considerations

Many factors may influence the results of the measurements. These factors need to be understood as good as possible in order to minimize their influence on the measurements, or at least to keep their influence constant throughout all measurements.

Light leakage into the black box is one of these factors. The light leakage is measured with the same setup as the decay time, except that the measuring-PMT is moved away from the crystal and screened from it, so that it will only measure leakage photons. This will give the number of leakage photons per trigger pulse read by the triggering-PMT. This rate can be directly compared to the rate of photons during measurements of the decay time to see if it gives a significant contribution. Light leakage was measured with the box covered by one and two blankets, aswell as uncovered, and the differences examined.

The calculated decay time may depend on

- The total number of single-photons measured.
- The data collection rate of single-photons, i.e. the number of single-photons per triggering pulse.
- The number of bins in the histogram used to fit the exponential function.
- The chosen start and end positions of the exponential fitting function.

These factors will be discussed in the following sections.

2.2.6 Number of Single-Photons

The delayed coincidence method has a low data collection rate. Accurate measurements performed by this method requires at least 100 000 data points, which could take several days [45]. Even for improved versions of the original method, a trade-off between collection time and amount of collected data needs to be made. To gain a good overview of how the number of collected single-photons influences the accuracy of the results, measurements with one to four million single-photons were taken for a few different crystals. These data sets could be split into several data sets with a lower number of single-photons and be compared to the results of the original data set. The procedure is summarized below:

1. Record a measurement with e.g. two million single-photons.
2. Calculate the decay time for the resulting histogram.
3. Split the original data file into ten data files, each containing data of 200 000 single-photons.
4. Calculate the decay time for each of the ten resulting histograms.
5. Find the average and the standard deviation of the ten decay times.
6. Repeat step 3 to 5 for different number of data files and single-photons.
7. Plot the average decay time and the standard deviation as a function of the number of single-photons.

This plot will indicate a limit above which increasing the number of measured single-photons will not significantly improve the accuracy of the results.

2.2.7 Data Collection Rate

To see how the data collection rate influences the calculated decay time, measurements were taken with different collection rates. Ten measurements were taken for each rate, and the average and standard deviation was calculated. The resulting calculated decay time was then plotted as a function of the collection rate.

2.2.8 Number of Bins and Exponential Fitting

The number of bins in the pulse shape histogram could influence the calculated decay time. To check if this was the case, the decay time of a few data sets was calculated for a range of bin numbers. The calculated decay times was then plotted as a function of the number of bins.

The start and end point for the exponential fitting influence the calculated decay time. The decay time of an LYSO crystal was calculated for a number of different end points. The results were plotted as a function of the end point. The choice of start and end points for the exponential fitting for both BGO and LYSO crystals is commented in Chapter 4.

2.3 Measurement of Energy Resolution

2.3.1 Method Overview

To find the energy resolution of different crystals, energy spectra are needed. These have been obtained by integrating each signal pulse. The integral is proportional to the energy deposited in the detector. For each pulse, this value is plotted in a histogram. This histogram represents an energy spectrum where the energy resolution can be found.

2.3.2 Experimental Setup

The energy resolution measurements and the decay time measurements are done simultaneously. The setup is illustrated in Figure 2.1. For the energy resolution measurements, only the triggering-PMT is necessary. This PMT detects the light pulses from the scintillator crystal. For decay time measurements, this pulse is used to create a zero-time signal. For energy resolution measurements, the signal is integrated to find the total charge. The total charge from the PMT is proportional to the energy deposited in the crystal. This information is used to create a pulse height spectrum, or energy spectrum.

The energy resolution has also been measured with an MPPC. The triggering-PMT is then substituted by an MPPC. The MPPC is directly connected to a current-to-voltage amplifier. The amplified signal is then read by the ADC.

2.3.3 Calculation of Energy Resolution

To calculate the energy resolution, a Gaussian function is fitted to the photopeak of the energy spectrum. This gives a value for the amplitude of the peak, $E_{\max}$, the position of the peak along the x-axis, E_0, and its standard deviation, σ. The energy resolution, calculated as the FWHM, can then be found according to Equation (1.13) and (1.14). This gives the energy resolution of the whole detector system. The intrinsic energy resolution of the scintillator crystals has not been found.

2.3.4 Determination of Uncertainties

Determination of uncertainties in the measurement of energy resolution is performed in a similar way as with the uncertainties in the decay time.

Measurements have been performed on the same BGO and LYSO crystals as when finding the uncertainties in the decay time.

2.3.5 Intrinsic Radioactivity of LYSO

The self-count of LYSO has a rate of 39 cps/g. For 5x5x20 mm^3 LYSO crystals, this results in a rate of about 144 cps. For 2x2x16 mm^3 crystals, this rate is about 19 cps. When measuring with a radioactive source, a certain fraction of the triggers measured actually come from the radioactivity of the crystal itself. The resulting pulse height spectrum will therefore also consist of data from the crystal itself. For a normal detector system (i.e. a PET scanner), the activity from small crystals is negligible compared to the activity of the source of interest. It would be desirable to check if this was also the case during these measurements. Even though the activity of the radioactive source and the crystal used is known, it is not trivial to estimate the contribution from the crystal's radioactivity quantitatively. The triggering system of the ADC runs continuously, but it is only capable of capturing about 500 trigger events per second. Therefore, not all the scintillation pulses from the crystal are actually read. Several approaches were tested in order to find the fraction of triggers measured as a consequence of the internal radioactivity of the LYSO crystals.

The basic idea to obtain this is to do one measurement without the radioactive source. Consequently, all counted triggers will then arise from the radioactivity of the crystal itself, in addition to the natural background radiation. Then, a measurement with the radioactive source is made. Each counted trigger then arises from either the radioactive source or the crystal itself. If the measurement setup was able to measure all the scintillation pulses from the crystal, subtracting the energy spectrum histogram of the first measurement from the last measurement would give the spectrum from the source only. Due to the rate limit of the ADC, the spectra cannot be directly compared. The ADC is, however, capable of counting a large number of triggers per second, even though it cannot read the signal of all of them. This can be utilized to find the energy spectrum resulting from the radioactive source only.

The ADC continously samples the signal from the photodetector, and stores it to a circular buffer. When the signal is larger than the threshold limit, the ADC will send the buffer content to the next unit in the signal processing system. In this case, that would be the PC with the LabView software. Meanwhile, the ADC is not able to process and forward an-

other event. By comparing the total number of counted triggers from the two measurements, the count rate introduced by the radioactive source can be found. As it turns out, this counting feature in the ADC is poorly implemented, and has a significant dead time. This method could therefore not be used.

The second approach involves using an external counter instead of the internal counter of the ADC to count the total number of triggers. This may be done by splitting the signal from the photodetector by using a Linear Fan-In/Fan-Out device[3]. The output of this device is two signals equal to the input signal. An external triggering device is also needed to ensure consistent triggering. The problem that arose with this approach was that the availiable Fan-In/Fan-Out device did not produce an output signal that matched the input signal. The output signal was therefore not suitable for further signal processing.

The solution to the challenge of finding the influence of the internal radioactivity of the LYSO crystals was to visually compare an energy spectrum of the LYSO crystal with that of a BGO crystal, both measured with ^{137}Cs. This is not a quantitative approach, but it still gives useful information.

2.3.6 Linearity of the Spectrum

The linearity of the energy spectra measured has been investigated. The ^{137}Cs source emits gamma photons at 662 keV, whereas the ^{22}Na source emits gamma photons at 511 keV and 1275 keV. The 662 keV peak has been used as the reference peak. If the ratio between the channel number and the energy of a specific peak matches the ratio between the channel number and the energy of the reference peak, the spectrum shows good linearity. In other words, the spectrum shows good linearity if Equation (2.2) is satisfied.

$$\frac{\mathrm{Ch}_{662}}{662\ \mathrm{keV}} \approx \frac{\mathrm{Ch}_{511}}{511\ \mathrm{keV}} \approx \frac{\mathrm{Ch}_{1275}}{1275\ \mathrm{keV}} \tag{2.2}$$

where Ch_{662}, Ch_{511}, and Ch_{1275} is the channel numbers corresponding to the energy peak of 662 keV, 511 keV, and 1275 keV, respectively. If

$$a_{662} = \frac{\mathrm{Ch}_{662}}{662\ \mathrm{keV}}\ , \qquad a_{511} = \frac{\mathrm{Ch}_{511}}{511\ \mathrm{keV}}\ , \quad \text{and} \quad a_{1275} = \frac{\mathrm{Ch}_{1275}}{1275\ \mathrm{keV}} \tag{2.3}$$

[3]LeCroy Model 428F Quad Linear Fan-In/Fan-Out

the deviation, dev, from linearity can be found, expressed in percentage, by Equation (2.4).

$$\text{dev} = \frac{|a_{662} - a_{511}|}{a_{662}} \cdot 100\% \tag{2.4}$$

The energy of ^{137}Cs, 662 keV, is used as the reference energy. The linearity and the deviation has been investigated both for the 511 keV and the 1275 keV peak.

2.3.7 Interaction Efficiency

For PET applications, all the gamma photons have an initial energy of 511 keV. When all of the energy of a gamma photon is deposited in the crystal, the event contributes to the photopeak, or full-energy peak, of the energy spectrum. Gamma photons contributing to the lower parts of the spectrum, e.g. the Compton continuum, have either undergone interactions in the tissue, or their energy is not fully deposited in the detector. The main interest is on the photons that contribute to the photopeak. The fraction of events contributing to the photopeak compared to the total number of events in the spectrum gives information on the interaction efficiency in the crystal. Generally, a larger crystal would give a higher interaction efficiency.

The interaction efficiency versus crystal size has been investigated. For this, the energy spectra from the different crystals have been used. The number of counts in the photopeak, n_{photo}, has been found and divided by the total number of counts, n_{total}, in the spectrum. Equation (2.5) shows the equation used. PF is the photofraction, i.e. the fraction of counts in the photopeak.

$$\text{PF} = \frac{n_{\text{photo}}}{n_{\text{total}}} \cdot 100\% \tag{2.5}$$

This does not give a quantitative measure of the detection efficiency in the different crystals. It is merely a way to compare the efficiencies of crystals of different sizes relative to each other. Since all the BGO crystals are the same size, the interaction efficiency has only been investigated for the LYSO crystals.

Chapter 3

Results

In this chapter, the results of the experimental work will be presented. The results and the uncertainties are measured under certain conditions. This includes the size of the data sets, data collection rate, fitting parameters and others. These conditions are outlined in Section 3.3.

3.1 Measurement of Decay Time

The decay time has been measured for all crystals listed in Table 2.1. The BGO curves are well fitted with a single-exponential curve from about 100 ns. The BGO crystals show decay times in the range of about 298 to 318 ns. All LYSO scintillator pulse shapes seem to be fitted well by a single-exponential decay curve. The LYSO crystals show decay times in the range of about 46 to 52 ns.

3.1.1 Decay Time of BGO Crystals

The literature value of the decay time of BGO crystals is 300 ns. Table 3.1 summarizes the results for all of the BGO crystals measured in this work. The results are mostly in good accordance with the expected value, although some variations between the different crystals are found. Figure 3.1a shows a typical pulse from the measurements performed on the BGO crystals. The bi-exponential shape of the scintillation pulse is especially apparent when using a logarithmic y-axis, as in Figure 3.1b. It can be seen as a change in the slope in the upper part of the pulse. The decay time of this component has not been found.

Table 3.1: Decay times of all BGO crystals. The decay times are calculated with 600 ns as the end point for the exponential fitting. The start point is set to 100 ns because of the bi-exponential nature of the pulse. The data set contains 200 000 single-photons measured with a rate of 1.0 photons per trigger.

Crystal	Decay time [ns]	Crystal	Decay time [ns]
SSB-5-20-1	303 ± 3	SSB-5-20-6	301 ± 3
SSB-5-20-2	307 ± 3	SSB-5-20-7	298 ± 3
SSB-5-20-3	303 ± 3	SSB-5-20-8	318 ± 3
SSB-5-20-4	300 ± 3	SSB-5-20-9	309 ± 3
SSB-5-20-5	301 ± 3	SSB-5-20-10	311 ± 3

Repeated measurements on the same crystals show a standard deviation in the calculated decay time of 3 ns. When measuring and calculating the decay time for all the ten BGO crystals, an average value of 305 ± 6 ns is found. The uncertainty due to repositioning is negligible for the BGO crystals.

3.1.2 Decay Time of LYSO Crystals

Table 3.2 summarizes the results for all of the LYSO crystals. The longest crystals (7x7x40 mm^3) shows the longest decay times. The shortest decay times have been measured for the smallest crystals (2x2x16 mm^3). One exception is the decay time of the GE-10-20-2 crystal, which has been measured to be 45.9 ± 0.2 ns. A typical measured decay curve of an LYSO crystal is shown in Figure 3.2.

A large measurement (2 million single-photons) was performed on crystal SSL-5-20-1 and crystal SSL-2-16-2 to quantify the standard deviation in the decay time for a single crystal without the influence of repositioning the crystal between measurements. For the two LYSO crystals SSL-5-20-1 and SSL-2-16-2, this standard deviation was calculated to be $\sigma_{\text{stat}} = 0.12$ ns and $\sigma_{\text{stat}} = 0.11$ ns, respectively. The standard deviation resulting when performing ten subsequent measurements on the same crystal was also found. For the 5x5x20 mm^3 crystal this resulted in $\sigma_{\text{tot}} = 0.22$ ns. According to Equation (2.1), this gives a $\sigma_{\text{repos}} = 0.18$ ns. For the 2x2x16 mm^3, $\sigma_{\text{tot}} = 0.24$ ns, resulting in a $\sigma_{\text{repos}} = 0.21$ ns. The standard deviations are summarized in Table 3.3.

Different crystals of the same size show differences in decay time. Dif-

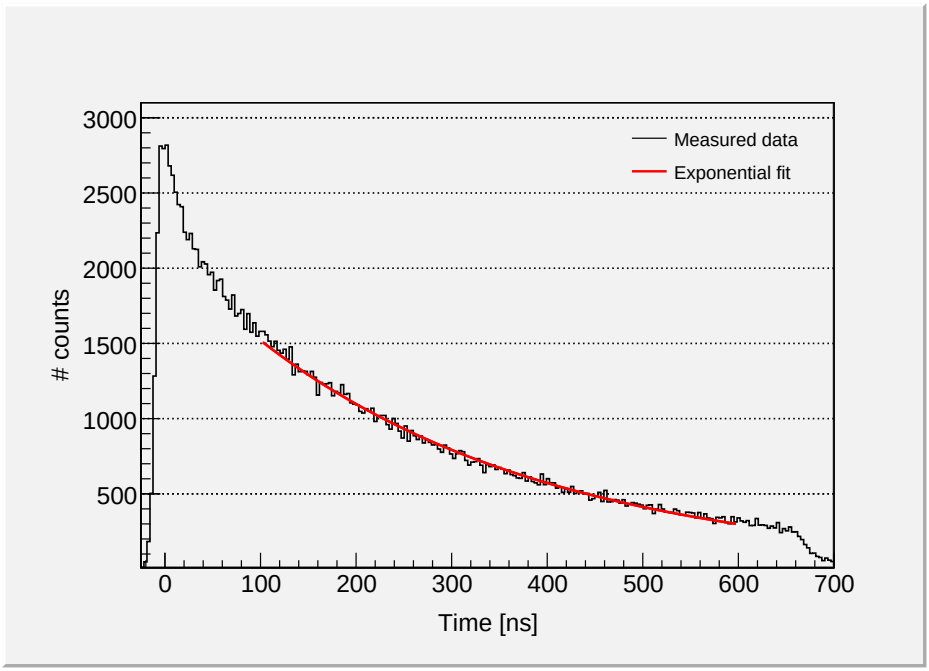

(a) Decay curve of BGO with a linear y-axis.

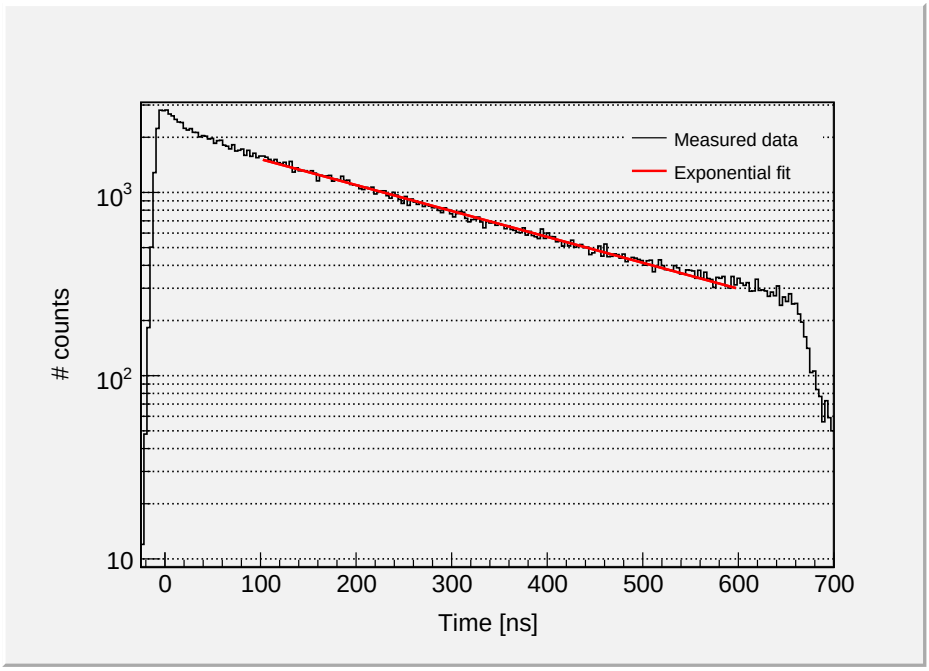

(b) Decay curve of BGO with a logarithmic y-axis. The change in the slope due to the bi-exponential nature of the pulse is especially apparent with a logarithmic scale.

Figure 3.1: Measured decay curve of BGO. These plots are from crystal SSB-5-20-2. The corresponding decay time is 301 ± 3 ns.

Table 3.2: Decay times of all LYSO crystals. The decay times are calculated with 160 ns as the end point for the exponential fitting on a data set with 200 000 single-photons measured with a rate of 1.0 photons per trigger.

Crystal	Decay time [ns]	Crystal	Decay time [ns]
SSL-5-20-1	48.0 ± 0.2		
SSL-5-20-2	48.2 ± 0.2		
SSL-5-30-1	49.5 ± 0.2	SSL-7-30-1	49.6 ± 0.2
SSL-5-30-2	49.4 ± 0.2	SSL-7-30-2	49.7 ± 0.2
SSL-5-40-1	49.7 ± 0.2	SSL-7-40-1	51.6 ± 0.2
SSL-5-40-2	49.5 ± 0.2	SSL-7-40-2	51.2 ± 0.2
GE-5-20-1	48.5 ± 0.2	GE-10-20-1	49.4 ± 0.2
GE-5-20-2	48.0 ± 0.2	GE-10-20-2	45.9 ± 0.2
SSL-2-16-1	46.4 ± 0.2	SSL-2-16-6	46.9 ± 0.2
SSL-2-16-2	46.7 ± 0.2	SSL-2-16-7	46.7 ± 0.2
SSL-2-16-3	47.4 ± 0.2	SSL-2-16-8	46.8 ± 0.2
SSL-2-16-4	47.4 ± 0.2	SSL-2-16-9	47.0 ± 0.2
SSL-2-16-5	47.1 ± 0.2	SSL-2-16-10	47.2 ± 0.2

Table 3.3: Standard deviations for LYSO crystals. The standard deviation due to statistics, σ_{stat}, and the total standard deviation, σ_{tot}, are measured directly. The standard deviation due to repositioning of the crystals, σ_{repos}, is calculated using Equation (2.1).

Crystal	σ_{stat} [ns]	σ_{tot} [ns]	σ_{repos} [ns]
SSL-5-20-1	0.12	0.22	0.18
SSL-2-16-2	0.11	0.24	0.21

ferences between the crystals should be as small as possible when building a large detector system containing a large number of crystals. The average decay time with standard deviation for the ten small (2x2x16 mm^3) crystals is 47.0 ± 0.3 ns. For the other LYSO crystals, this number cannot be calculated since there are only two crystals of each size.

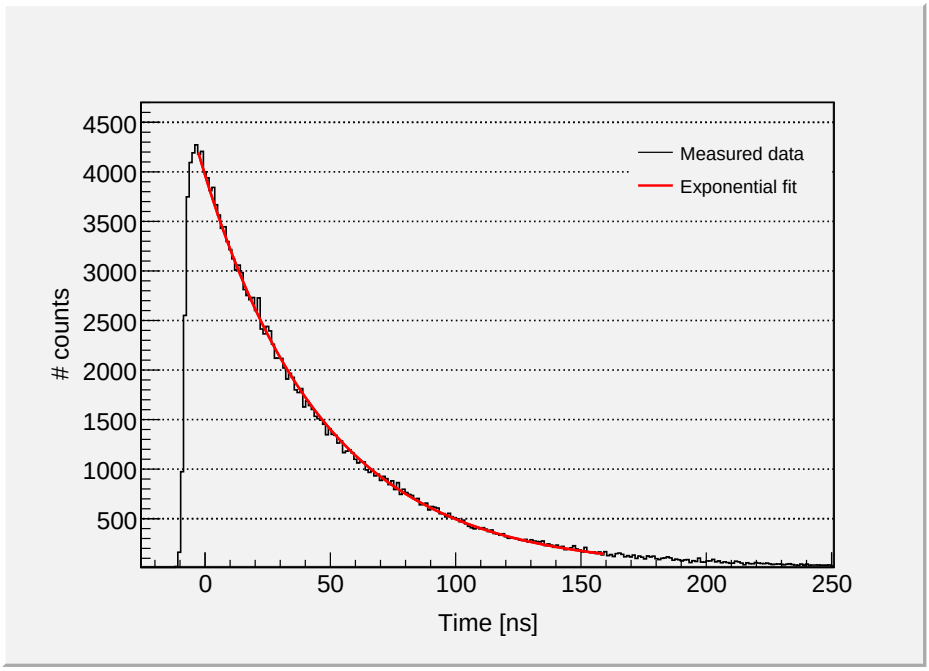

Figure 3.2: Measured decay curve of LYSO. This plot is from crystal SSL-5-20-1. The corresponding decay time is 48.0 $\pm$ 0.2 ns.

3.2 Measurement of Energy Resolution

The energy resolution has been measured for all crystals listed in Table 2.1 without the use of optical grease. Measurements with optical grease has been performed with one BGO crystal (SSB-5-20-5), and three LYSO crystals (GE-5-20-2, SSL-2-16-2, SSL-7-40-1). Comparing BGO and LYSO crystals of the same size shows that LYSO has a much better energy resolution. Without optical coupling, the 5x5x20 mm^3 BGO crystals show an energy resolution in the range of 20% to 22%. LYSO crystals of the same size show an energy resolution of about 13% to 15.5%. With the best optical coupling, the BGO crystal has been measured with an energy resolution of 16.6 $\pm$ 0.1%. The corresponding value for the LYSO crystal GE-5-20-2 is 11.4 $\pm$ 0.1%. All energy resolution measurements are based on data from channels corresponding to an energy of 662 keV.

The energy resolution of one crystal, GE-5-20-2, has also been measured with an MPPC, both with and without optical grease. The resulting energy resolution is somewhat poorer for the setup with the MPPC than with the PMT.

Table 3.4: Energy resolutions of all BGO crystals without optical grease.

Crystal	Energy resolution [%]	Crystal	Energy resolution [%]
SSB-5-20-1	21.1 ± 0.1	SSB-5-20-6	21.3 ± 0.1
SSB-5-20-2	21.8 ± 0.1	SSB-5-20-7	22.1 ± 0.1
SSB-5-20-3	21.7 ± 0.1	SSB-5-20-8	21.5 ± 0.1
SSB-5-20-4	20.9 ± 0.1	SSB-5-20-9	21.0 ± 0.1
SSB-5-20-5	20.1 ± 0.1	SSB-5-20-10	20.4 ± 0.1

Table 3.5: Energy resolution of BGO crystals with optical grease.

Crystal	Energy resolution [%]		
	BC-630	GC-0608	No grease
SSB-5-20-5	16.6 ± 0.1	18.3 ± 0.1	20.1 ± 0.1

3.2.1 Energy Resolution of BGO Crystals

Table 3.4 summarizes the results for all of the BGO crystals without optical grease. The BGO crystals show energy resolutions in the range of about 20% to 22% without optical grease. The average energy resolution of the ten BGO crystals is $21.2 \pm 0.6\%$.

The energy resolution has also been measured with the use of optical grease on one BGO crystal. The energy resolution is significantly improved, to $16.6 \pm 0.1\%$, with the use of the BC-630 optical grease. With the GC-0608 optical grease, the energy resolution has been measured to be $18.3 \pm 0.1\%$. The results are shown in Table 3.5. A typical energy spectrum measured for a BGO crystal is shown in Figure 3.6b.

The linearity of the energy spectra measured with BGO crystals is very good. Following Equation (2.4), the deviation is less than 1% for the 511 keV and the 1275 keV peaks, relative to the 662 keV peak.

3.2.2 Energy Resolution of LYSO Crystals

Table 3.6 summarizes the results for all of the LYSO crystals without optical grease. The smallest LYSO crystals (2x2x16 mm^3) show energy resolutions in the range of 13.5% to 16.5%. The 10x10x20 mm^3 crystals do not fit into the PMT window, resulting in poor light transmission from

Table 3.6: Energy resolution of LYSO crystals without optical grease. The uncertainties for the 2x2x16 mm^3 crystals are determined by the standard deviation from ten measurements on crystal SSL-2-16-2. The uncertainties for the rest of the crystals are determined by transferring the uncertainty from the SSL-5-20-1 crystal.

Crystal	Energy resolution [%]	Crystal	Energy resolution [%]
SSL-5-20-1	14.0 ± 0.1		
SSL-5-20-2	13.6 ± 0.1		
SSL-5-30-1	14.7 ± 0.1	SSL-7-30-1	14.6 ± 0.1
SSL-5-30-2	14.5 ± 0.1	SSL-7-30-2	14.9 ± 0.1
SSL-5-40-1	15.0 ± 0.1	SSL-7-40-1	15.1 ± 0.1
SSL-5-40-2	15.5 ± 0.1	SSL-7-40-2	14.6 ± 0.1
GE-5-20-1	13.3 ± 0.1	GE-10-20-1	17.0 ± 0.1
GE-5-20-2	13.4 ± 0.1	GE-10-20-2	19.6 ± 0.1
SSL-2-16-1	15.4 ± 0.2	SSL-2-16-6	14.8 ± 0.2
SSL-2-16-2	13.8 ± 0.2	SSL-2-16-7	16.4 ± 0.2
SSL-2-16-3	14.8 ± 0.2	SSL-2-16-8	14.0 ± 0.2
SSL-2-16-4	14.8 ± 0.2	SSL-2-16-9	15.0 ± 0.2
SSL-2-16-5	15.6 ± 0.2	SSL-2-16-10	15.2 ± 0.2

the crystal to the PMT. This results in an energy resolution of 17.0 ± 0.1 % and 19.6 ± 0.1 % for the GE-10-20-1 and the GE-10-20-2 crystals, respectively. The other LYSO crystals show energy resolutions in the range of about 13% to 15.5% without optical grease. A typical energy spectrum measured for a 5x5x20 mm^3 crystal is shown in Figure 3.3a. An energy spectrum of a 2x2x16 mm^3 crystal is shown in Figure 3.3b. It is evident that less scintillation light is incident on the photodetector when measuring on the smallest crystals. This can be seen by comparing the channel number corresponding to the photopeaks in the to plots of Figure 3.3. The result of less light is a degraded energy resolution.

For the ten 2x2x16 mm^3 crystals, the average measured energy resolution is 15.0 ± 0.7% measured without optical grease. Again, when building a large system, this variation between crystals should be as small as possible.

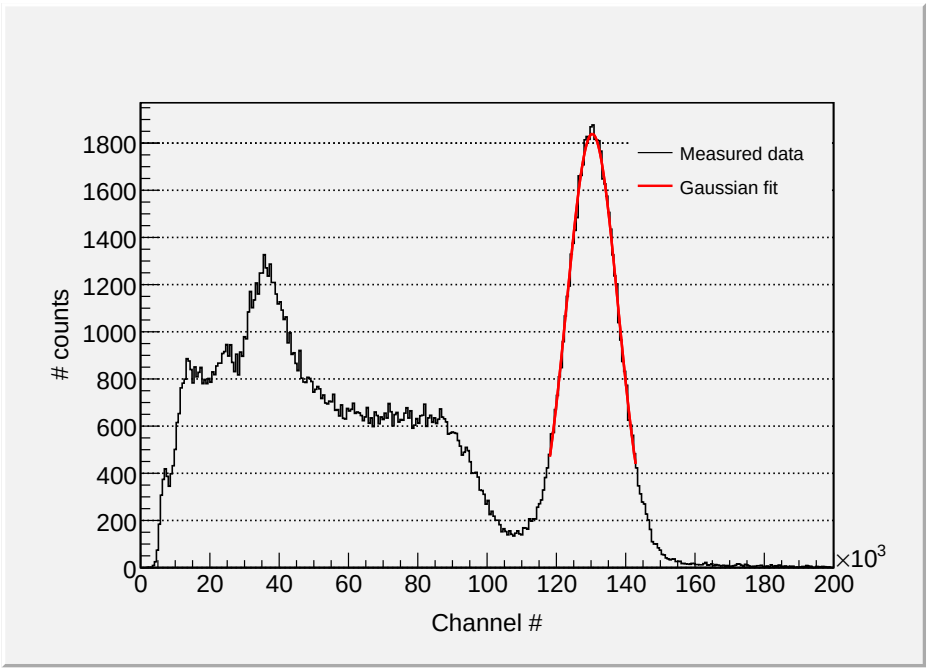

(a) Energy spectrum of the GE-5-20-2 crystal without optical grease. The corresponding energy resolution is 13.4 ± 0.1%.

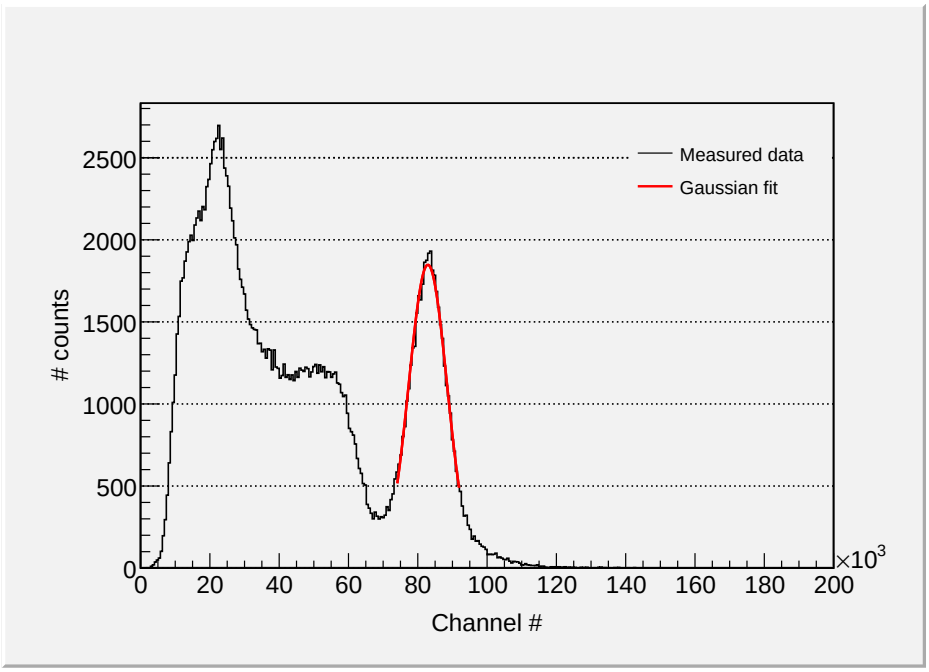

(b) Energy spectrum of the SSL-2-16-2 crystal without optical grease. The corresponding energy resolution is 15.7 ± 0.2%.

Figure 3.3: Energy spectra of two different LYSO crystals. The amount of scintillation light detected from the larger crystal is considerably higher than from the smaller one. This results in a better energy resolution for the large crystal.

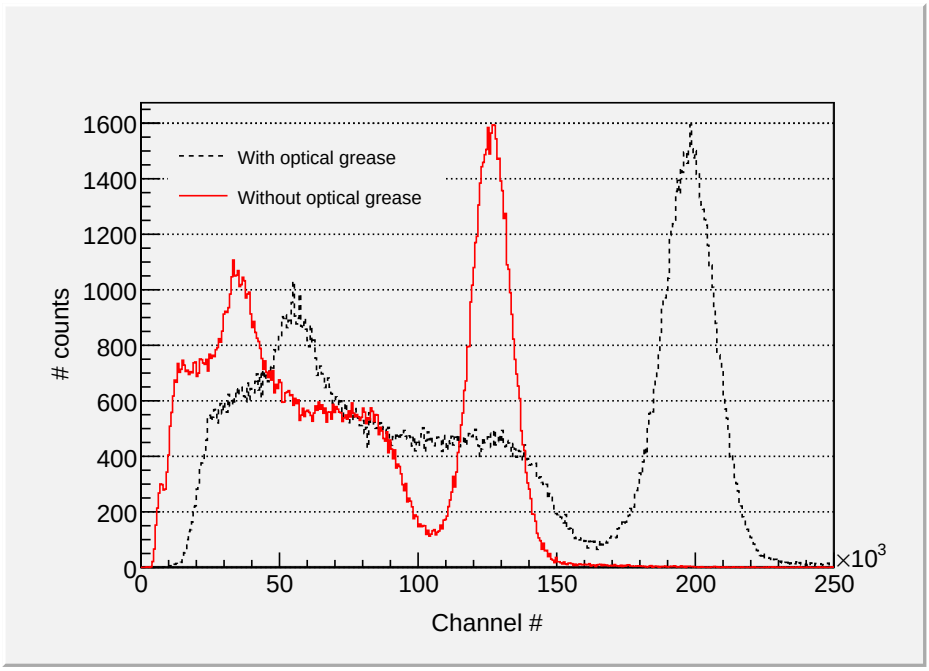

Figure 3.4: Energy spectra of the GE-5-20-2 crystal with and without optical grease. The corresponding energy resolutions are 11.4 ± 0.1% and 13.4 ± 0.1%. The plots have been normalized to matching peak height. Optical grease used: BC-630.

The energy resolution of three LYSO crystals has been measured with optical grease. The results are shown in Table 3.7. There is no clear evidence to state that one of the two types of optical grease is superior to the other. Figure 3.4 shows energy spectra both with BC-630 and without optical grease for the same crystal. As expected, the energy resolution increases when optical grease is used. When measured with grease, the total energy spectrum is shifted to the right, and the peak shows a more narrow FWHM value. The improvement is less for the smallest crystal than for the two larger ones.

The energy resolution of the GE-5-20-2 crystal has also been measured using an MPPC. The results are shown in Table 3.8 together with the results from the PMT measurements on the same crystal. The energy resolution obtained with the MPPC is poorer than that obtained with the PMT.

Figure 3.5a shows the energy spectrum resulting when measuring on an LYSO crystal without a radioactive source. An energy spectrum measured with a radioactive source is shown for reference (Figure 3.5b). The

Table 3.7: Energy resolution of LYSO crystals with the two types of optical grease. The results for the same crystals without optical grease is included for easy comparison.

Crystal	Energy resolution [%]		
	BC-630	GC-0608	No grease
GE-5-20-2	11.4 ± 0.1	11.5 ± 0.1	13.4 ± 0.1
SSL-2-16-2	13.3 ± 0.2	–	13.8 ± 0.2
SSL-7-40-1	12.8 ± 0.1	12.3 ± 0.1	15.1 ± 0.1

Table 3.8: Energy resolution of LYSO crystal measured with an MPPC. The results for the same crystal measured with a PMT is included for easy comparison.

Crystal	Energy resolution with MPPC [%]		Energy resolution with PMT [%]		
	BC-630	No grease	BC-630	GC-0608	No grease
GE-5-20-2	12.2 ± 0.1	14.2 ± 0.1	11.4 ± 0.1	11.5 ± 0.1	13.4 ± 0.1

channel numbers of the two plots are comparable, but the amplitudes are not. The long tail on the right in the upper plot is completely suppressed in the lower plot. This suggests that the excitation of the crystal due to self-count is negligible compared to the excitation caused by the radioactive source when it is present. The energy spectrum of a BGO and an LYSO crystal has also been compared to see if the internal radioactivity of the LYSO crystals effects the spectrum measured with a radioactive source. The spectra are shown in Figure 3.6, with LYSO on top and BGO at the bottom. By visual inspection, the two spectra are very similar in shape, again suggesting that the internal radiation is negligible.

The linearity of the spectra is very good for the 5x5x20 mm^3 LYSO crystal that has been tested. Equation (2.4) gives a deviation of less than 2% both for the 511 keV and the 1275 keV peak. Figure 3.7 shows a spectrum from the ^{137}Cs and the ^{22}Na source. All three expected peaks are visible in the spectrum.

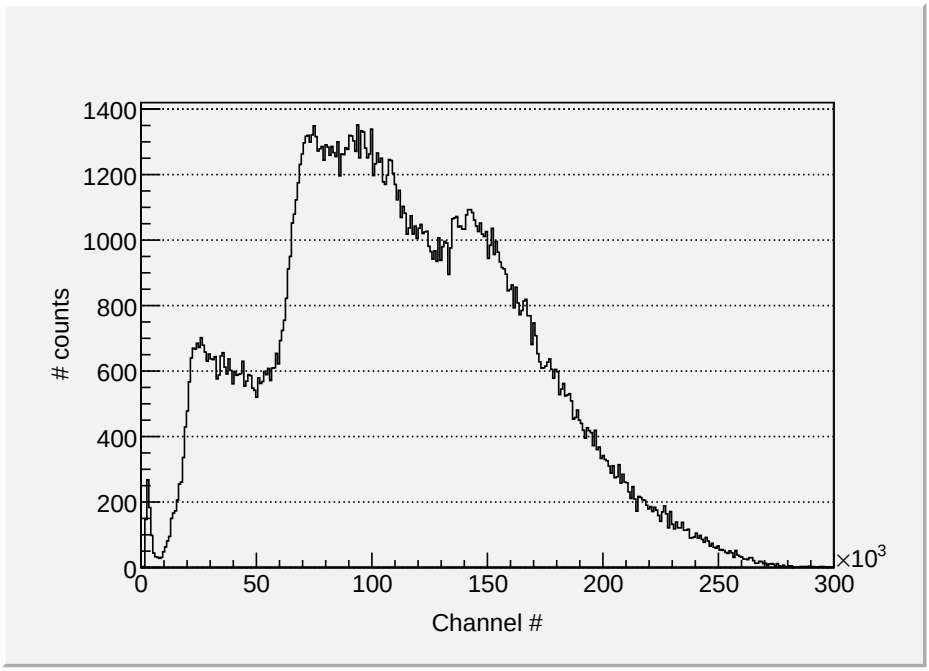

(a) Energy spectrum of LYSO without a radioactive source (self-count only).

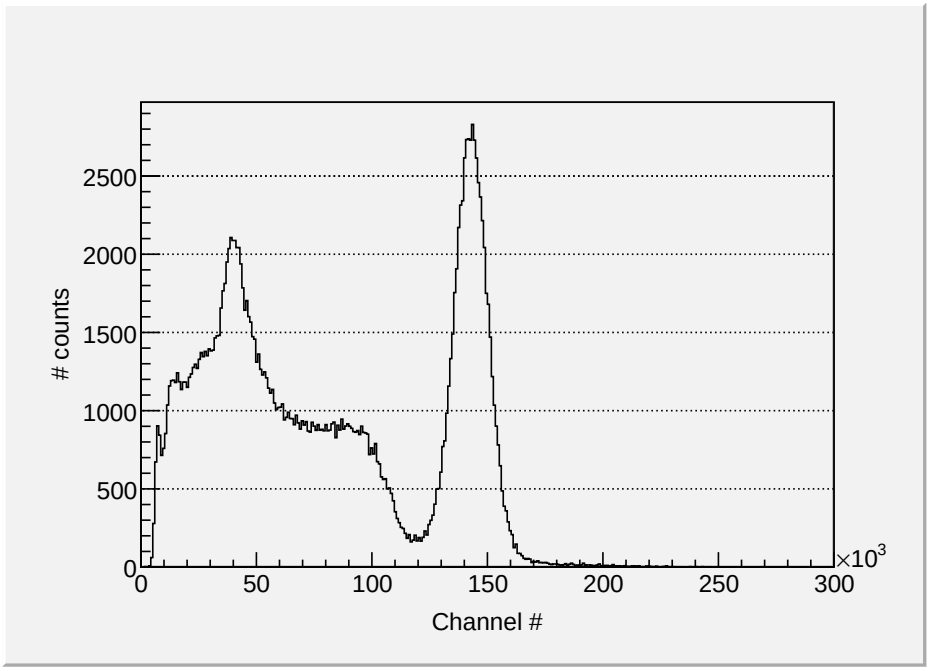

(b) Energy spectrum of LYSO with ^{137}Cs source.

Figure 3.5: Energy spectra of LYSO without and with the ^{137}Cs source. The rate of the self-count is too low to have an influence on the spectrum obtained with the radioactive source present.

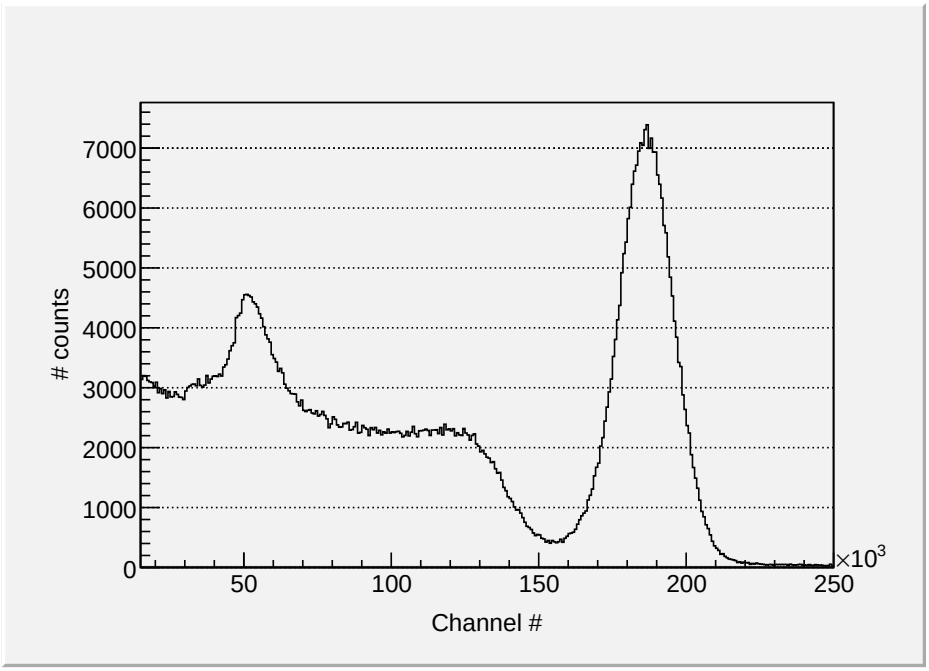

(a) Energy spectrum of LYSO.

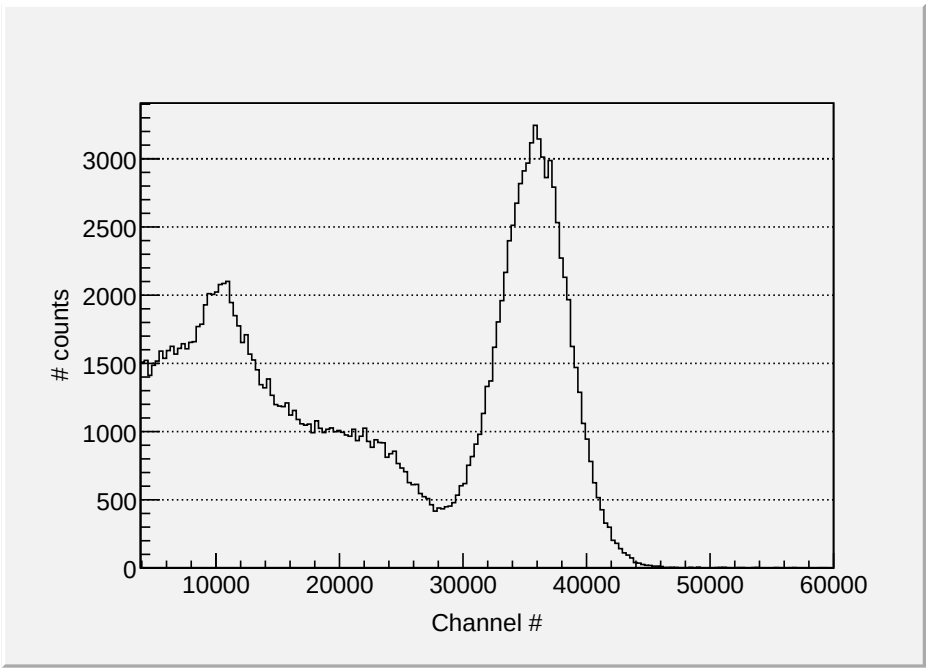

(b) Energy spectrum of BGO.

Figure 3.6: Energy spectra of LYSO and BGO. The similarity of the two spectra is evident. The differences in light output from BGO and LYSO is the reason for the different x-axes. The difference in the y-axes is due to the different number of data points in these particular plots.

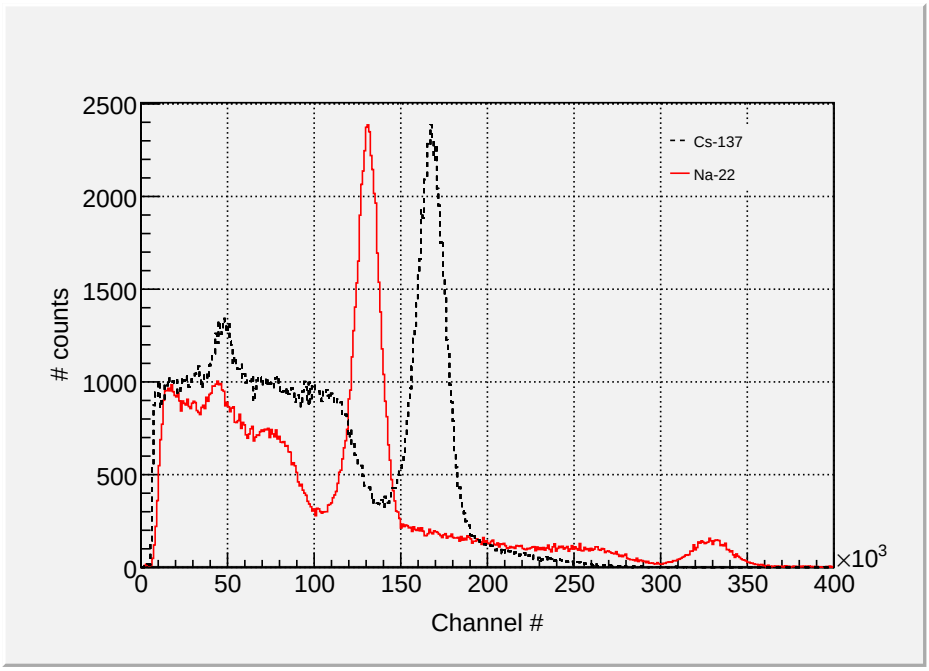

Figure 3.7: Energy spectrum showing both ^{137}Cs and ^{22}Na. The spectrum shows very good linearity. The plot has been normalized so that the amplitude of the 511 keV peak and the 662 keV peak are equal. The peak at 1275 keV from the ^{22}Na source is also visible at the right end of the spectrum.

The interaction efficiency has been investigated for LYSO crystals of different sizes. The method gives an indication of the interaction efficiency of crystals with different sizes relative to each other. It is not a quantitative determination. No differences were found between the 5x5 mm^2 crystals of different lengths (20 mm, 30 mm, and 40 mm). The same was true for the 7x7 mm^2 crystals. The thickness of the crystal influences the photofraction. The photofraction of the smallest crystals was calculated to about 23%. For the 5x5 mm^2 and the 7x7 mm^2 crystals it was calculated to be about 35% and 40%, respectively. The 10x10 mm^2 crystals had a photofraction of about 51%. The photofractions are calculated by Equation (2.5). Figure 3.8 shows a plot of the interaction efficiency as a function of crystal thickness. It is obvious that increasing the thickness of the crystal increases the amount of counts in the photopeak.

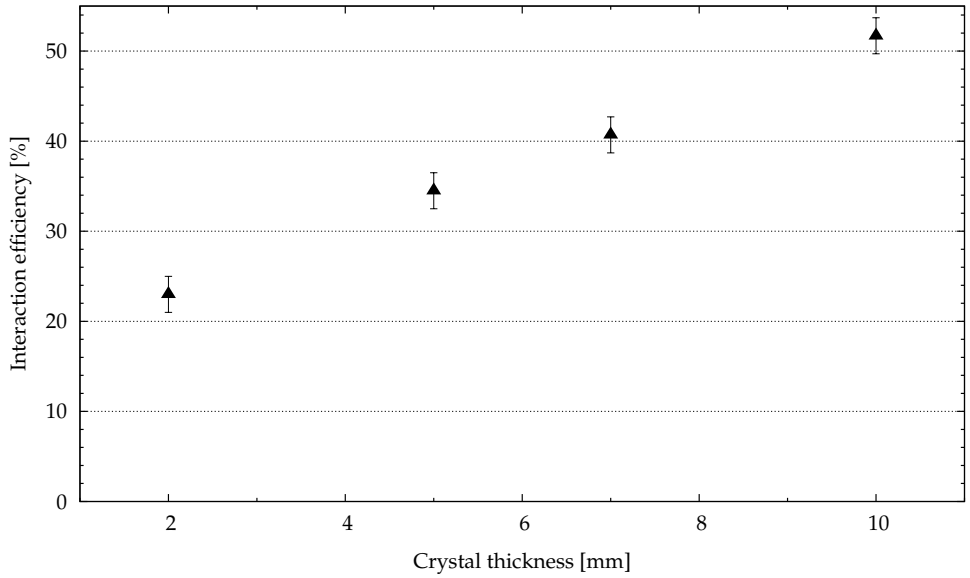

Figure 3.8: Interaction efficiency of different crystals. The result is not a quantitative measure of the absolute interaction efficiency, but rather just a way to compare the efficiency of crystals of different sizes.

3.3 Measurement Parameters

3.3.1 Data Collection

Because of the relatively low data collection rate of these measurements, it has been important to gain an overview of how much data is needed to obtain results with a good accuracy. The method used to gain this overview is described in detail in Section 2.2.6.

Figure 3.9 shows a plot of the average decay time as a function of the number of single-photons measured. The error bars are plus-minus one standard deviation of the average decay time. The so-called 'true' value of the decay time is the decay time calculated from the whole data set. In Figure 3.9, this value is shown by the dotted line. On the basis of these and similar plots, a data collection amount of 200 000 single-photons was chosen in the main measurements in this thesis.

The data collection rate, i.e. the number of single-photons collected per trigger, influences the calculated decay time. Figure 3.10 shows the calculated decay time as a function of this rate. A rate close to 1.0 photons/event has been used for the measurements presented here.

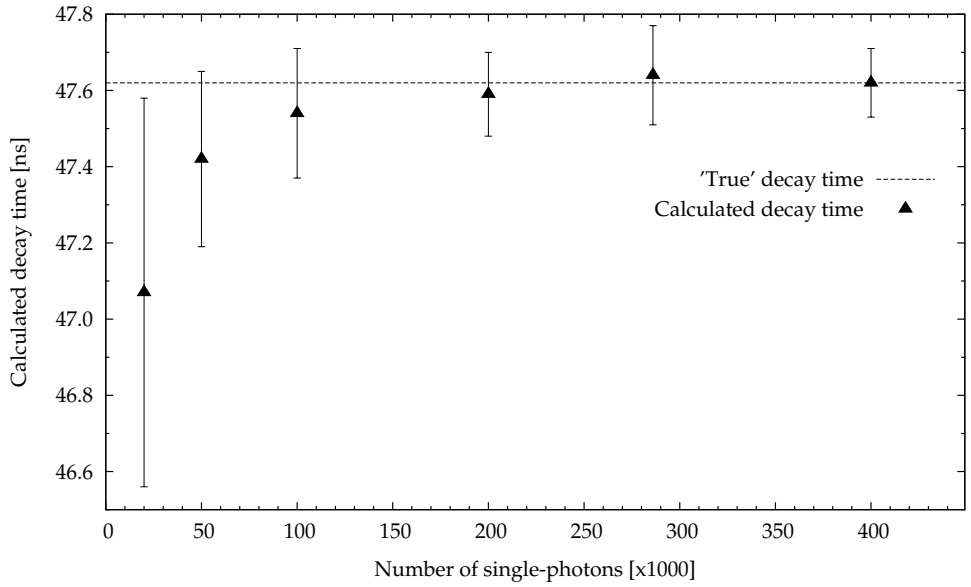

Figure 3.9: Decay time versus number of single-photons. The 'true' decay time is calculated on the basis of a data set of two million single-photons. Above a certain amount, the number of single-photons in the data set does no longer affect the calculated decay time significantly.

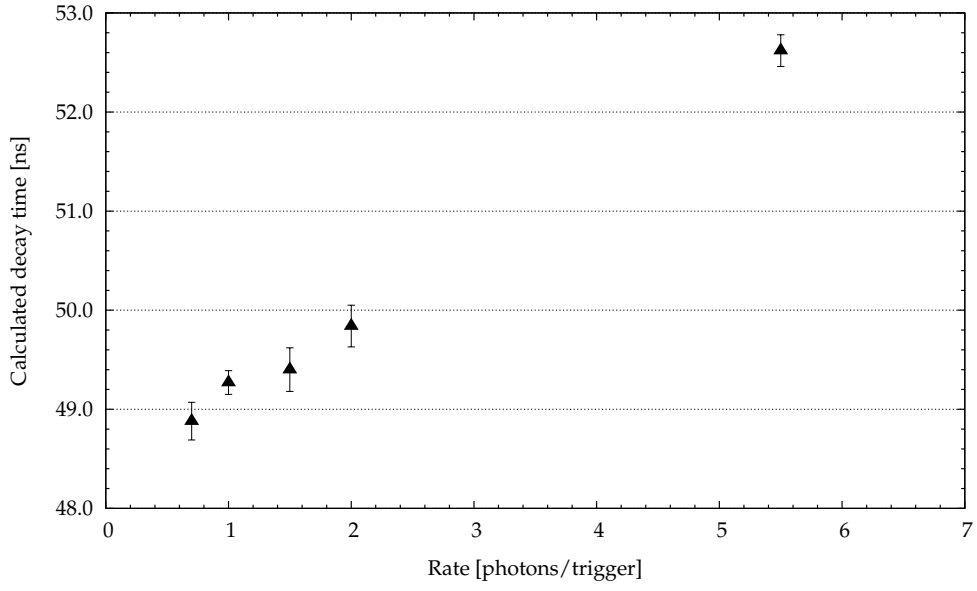

Figure 3.10: Decay time versus rate of single-photons. As the rate increases, the calculated decay time also increases.

3.3.2 Calculation of Decay Time

The calculated decay time for the LYSO crystals increases when the position of the end point for the exponential fit is increased. This is shown in Figure 3.11. Figure 3.12 shows a plot of the calculated decay time as a function of the number of bins in the pulse shape histogram. The plot shows that the number of bins does not affect the calculated result significantly within a large range of values.

3.3.3 Light Leakage

The light leakage into the black box was measured for three different configurations: the black box only, and the black box covered with one and two black blankets, respectively. The results are presented as the number of leakage photons per trigger pulse in the triggering-PMT. This makes it easy to compare the result to the rate of single-photons in the measuring-PMT during measurements. Table 3.9 summarizes the results with the minimum, maximum and typical leakage rate measured. The leakage rate measured without covering is typically lower early in the morning than during mid-day. The light leakage measurements clearly show that

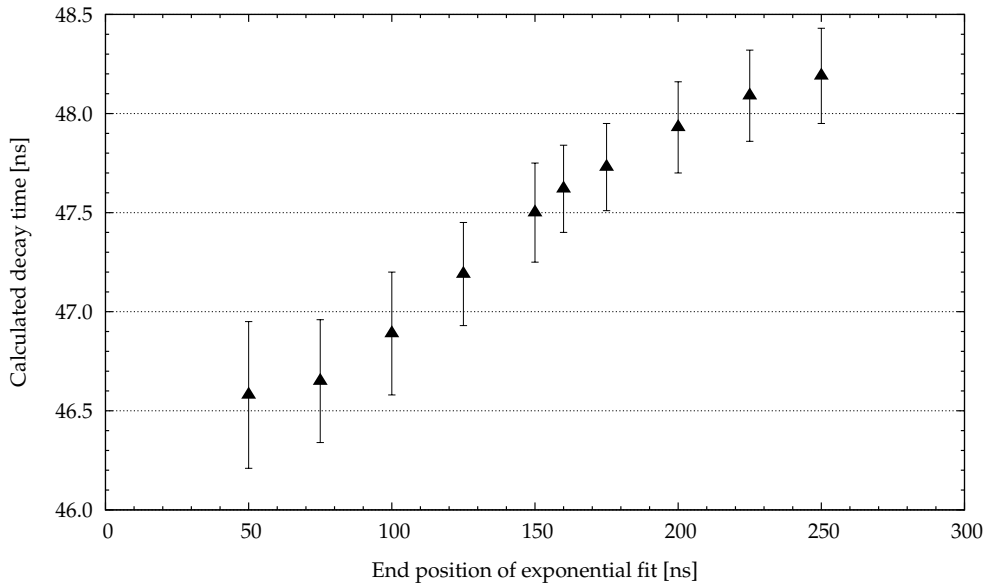

Figure 3.11: Decay time versus the end position for the exponential fitting function. The calculated decay time increases when the end position of the exponential fitting function is increased.

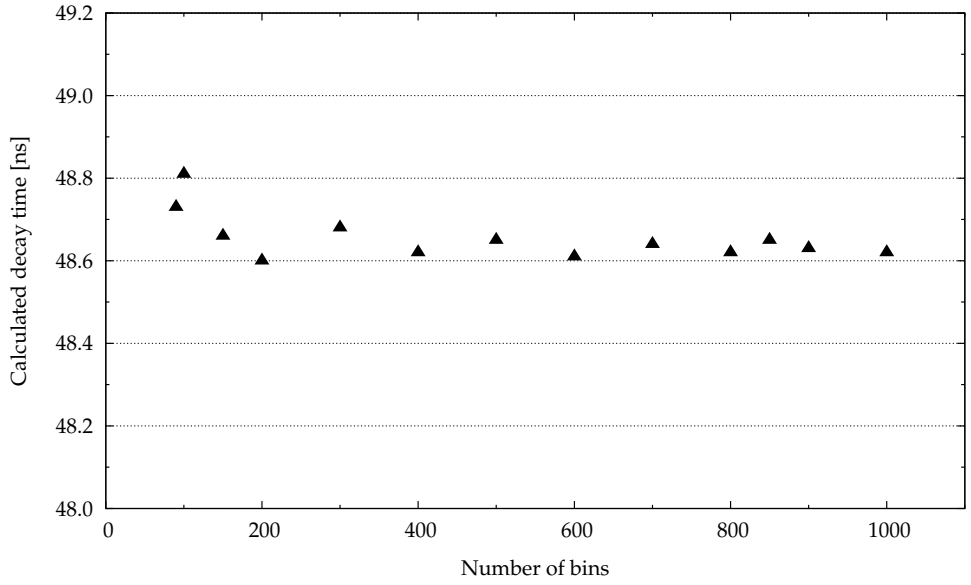

Figure 3.12: Calculated decay time as a function of the number of bins used in the pulse shape histogram when exponential fitting is performed.

Table 3.9: Light leakage measurements. The minimum, maximum and typical rate of the leakage light measured in the measuring-PMT is listed for different configurations of the black box: uncovered, covered with one blanket, covered with two blankets

Configuration of black box	Measured leakage rate [photons/trigger]		
	Min.	Max.	Typical
No blanket	0.07	0.36	0.25
One blanket	0.004	0.04	0.02
Two blankets	0.0008	0.003	0.002

the box is not sufficiently lightproof without extra covering. The values for 'typical' are determined on the basis of several measurements performed during mid-day on a bright but cloudy day. With a rate of 1.0 photon per trigger during measurements, typically one of four measured photons are actually leakage photons. The main measurements were performed with the black box covered by two blankets.

3.3.4 Density of Crystals

The calculated densities of the different crystals are listed in Table 3.10. The values can be compared to the values listed in Table 1.2. The density of the BGO crystals is within the values stated in literature and in the data sheet from the manufacturer. The density of LYSO crystals vary depending on the amount of yttrium. According to the manufacturer, the LYSO crystals used have a density of 7.3 g/cm^3. The values found are within the stated value, except for the 10x10x20 mm^3, which have been measured as slightly more dense than stated. No data sheet stating the amount of yttrium in the LYSO crystals could be obtained from the manufacturer. The measurements of crystal densities indicates that the amount is small. This is also evident from the fact that the stated density of the current crystals is higher than what is given in Table 1.2. The uncertainty for the smallest LYSO crystals is very high due to the high relative uncertainty in determination of the mass (about 20%).

Table 3.10: Density of crystals. The uncertainty in the crystal sizes is stated as 0.1 mm for all crystal sizes.

Crystal type	Size [mm^3]	Volume [cm^3]	Mass [g]	Density [g/cm^3]
BGO	5x5x20	0.500 ± 0.014	3.7 ± 0.1	7.4 ± 0.3
LYSO	5x5x20	0.500 ± 0.014	3.8 ± 0.1	7.6 ± 0.3
LYSO	2x2x16	0.064 ± 0.005	0.5 ± 0.1	7.8 ± 1.7
LYSO	10x10x20	2.00 ± 0.03	15.0 ± 0.1	7.5 ± 0.1

Chapter 4

Discussion

In the discussion, the main findings will be discussed along with the factors that might influence these results.

Decay Time

All ten BGO crystals used in the experiments are the same size, namely 5x5x20 mm^3. The average decay time of the main decay component in the BGO crystals has been measured as 305 ± 6 ns. This value is in accordance with the literature value of the decay time of BGO of 300 ns (see Table 1.2). Crystal SSB-5-20-8 shows the largest deviation from the literature value of the decay time: 318 ± 3 ns. This is a deviation of about 6%.

The value of the decay time for LYSO crystals is typically quoted as 40 or 41 ns (see Table 1.2). However, the data sheet for the SSL crystals used in this work gives a value of 50 ns. The decay times found for the different LYSO crystals are in the range of 45.9 to 51.6 ns. It is important to keep in mind that these values are measured with several parameters, such as the collection rate and the end point for the exponential fitting, fixed at specific values. Choosing different values for these parameters would cause different results. The wrapping in teflon tape also influences the measured decay time, as will be discussed below. This taken into account, the values for the decay time of the LYSO crystals are in fairly good accordance with the expected values.

Generally, the smaller LYSO crystals show a shorter decay time than the larger ones. This is probably due to the increased travel length for

the photons in the larger crystals. One exception is the decay time of the GE-10-20-2 crystal, which has been measured to 45.9 $\pm$ 0.2 ns. This is more than 3 ns shorter than for the same-sized GE-10-20-1 crystal. The decay time has been measured several times, and no obvious reason for the difference has been found. The most probable explanation seems to be differences in the crystals themselves.

Energy Resolution

The energy resolution presented in this work is the energy resolution of the whole detector system. The intrinsic energy resolution of the scintillation crystals has not been found. This would require to find the number of photoelectrons per energy unit by comparing the photopeak at 662 keV (for ^{137}Cs) with the single photoelectron peak [29]. By doing so, the light output can also be found. This has not been done, but would be an interesting task for further work. Even though the intrinsic energy resolution of the crystals is an interesting quantity, it is the energy resolution of the whole system that determines its applicability.

Some publications report an energy resolution for BGO crystals of about 10%, while others have found a resolution of 20% (see Table 1.2). The manufacturer has not stated any value for the energy resolution. The measurements performed here show an energy resolution of about 20% without the use of optical grease. With optical grease, a resolution of 16.6 $\pm$ 0.1% has been obtained. The gap to 10% is indeed large. Some of the difference might be due to the effort of optimization performed by Moszynski et al. [22], which has not been done here. It may also be due to different growth processes for the crystals.

Excluding the 2x2x16 mm^3 crystals, energy resolution seems to be degraded as the length of the LYSO crystals increases. Note that this has not been investigated in detail. The smallest crystals (2x2x16 mm^3) have worse energy resolution than the 5x5x20 mm^3 crystals. From Figure 3.3, it is clear that less scintillation light is produced by the smaller crystals. This might be because the small size reduces the amount of photoelectric absorption and increases the escape of Compton scattered photons from the crystal. The consequence is a degraded energy resolution.

The best energy resolution measured without optical grease has been obtained with the GE crystals coupled to a PMT. Therefore, the GE-5-20-2 crystal was tested with optical grease, and also coupled to an MPPC. The optical coupling increases the light transmission from the crystal to the

photodetector, and thus increases the energy resolution.

The energy resolution measured on the LYSO crystal with the PMT is superior to that measured with the MPPC. MPPCs have a higher quantum efficiency, and they are often said to give a better energy resolution than PMTs. The PMT has a large enough window to cover all of the end-side of the crystal. The MPPC only has an active area of 3x3 mm^2. When using a crystal with an end-side area of 5x5 mm^2, a large fraction of the light from the crystal will not reach the photodetector. This is most likely the main reason for the inferior energy resolution measured with the MPPC. Measuring on a 2x2x16 mm^3 crystal would have eliminated this factor. These smallest crystals are difficult to position in a controlled and reproducible way, especially coupled to the small MPPC, and the attempts did not succeed. When a more elegant fixation system is implemented in the black box, these measurements should be easier to carry out.

Moszynski et al. [22] also presents measurements where the total energy resolution of a detector with LSO crystals is better using a PMT than when using a large area avalanche photodiode (LAAPD). The reason why the resolution is not improved when using the LAAPD is suggested to be due to the large contribution of the intrinsic resolution of the crystals. In the same study, the energy resolution measured on a BGO crystal is significantly improved when measuring with the LAAPD compared to the PMT. This will be an interesting point to investigate in further work.

The interaction efficiency of crystals of different sizes was compared. The interaction efficiency is clearly dependent on the thickness of the crystal. When a Compton scattering occurs in the crystal, the incoming photon looses some of its initial energy and is deflected a certain angle. If the crystal is thin compared to the interaction length for the photon, the chances are high that the photon will escape the crystal. Its deposited energy then contributes to the lower parts of the energy spectrum. In a thicker crystal, the probability that the Compton scattered photon interacts multiple times is increased. This happens in a time scale so short that the system does not distinguish it as several events. Therefore, all the energy deposited from the same incoming gamma photon will be added, and the sum reaches the photopeak if the photon does not escape the crystal. A thicker crystal will ensure that fewer photons escape. No differences were found for crystals of the same thickness with different lengths. This is probably due to the fact that the interaction fraction is high already at 20 mm (see Table 1.3).

Uncertainties

The uncertainties in the decay time for the BGO and LYSO crystals have been found as ± 3 ns and ± 0.2 ns, respectively. These uncertainties have been found by doing ten measurements on one crystal, removing and repositioning the crystal between each measurement. The average decay time and the standard deviation of the measurements have then been calculated. Even though the 2x2x16 mm^3 crystals are more difficult to position correctly in the measurement setup, no differences in uncertainties were found between them and the 5x5x20 mm^3 LYSO crystals when it comes to decay time. This seems reasonable because the setup for measuring the decay time is not very vulnerable to differences in the (re)positioning of the crystals, as long as parameters like the collection rate is kept constant. Since the repositioning of the crystals contributes the most to the uncertainties (see Table 3.3), it is reasonable to believe that the uncertainty is transferable to the larger LYSO crystals as well.

The uncertainties in the energy resolution were calculated in the same way as described for the decay time. Here, the BGO and the LYSO crystals of the same size (5x5x20 mm^3) have the same absolute uncertainty, namely 0.1%. The measurement of energy resolution is more vulnerable to how the crystal is positioned, e.g. if good optical contact is achieved. This is also seen by the fact that the uncertainty for the smallest crystals is higher than for the others. It has been found to be 0.2%. An uncertainty of 0.1% has been assumed for the larger LYSO crystals since these are easy to position.

When measuring the energy resolution with optical gel, the smallest crystals, in particular, are easier to position. This could result in a lower uncertainty compared to the measurements without optical grease. It has not been investigated if this is the case. This would be of greater interest if the uncertainties without optical grease had been significantly larger. For now, the uncertainties calculated without the use of optical grease have been used for measurements with optical grease.

Some measurements performed indicate that the uncertainties stated for the energy resolution of the crystals are somewhat too small. This might be due to the fact that the results of the measurements are influenced by uncontrolled factors, such as e.g. the temperature. The temperature would typically be approximately constant during ten subsequent measurements, but could vary significantly from one day to another. The optical grease introduces another uncertainty factor: it is not possible to

ensure identical conditions each time the crystal is coupled to the photodetector. The exact amount of grease will vary, and it is also possible that air bubbles are incident in the grease. The latter will reduce the light transmission. It might be these kind of factors that result in BC-630 giving the best results for the energy resolution for two crystals (SSB-5-20-5 and GE-5-20-2), while GC-0608 gives the best result for one crystal (SSL-7-40-1). The uncertainties should therefore ideally be measured with the use of optical grease. On the other side, in a real system the crystal will be coupled to the photodetector only once. The amount of grease and of any possible air bubbles present will not vary in these circumstances.

Generally, the energy resolution gets better as the energy of the photons in question increases. All the measured energy resolutions have been found for the 662 keV peak of ^{137}Cs. Since the annihilation photons in PET applications have an energy of 511 keV, the achievable energy resolution is expected to be slightly poorer.

Number of Single-Photons

The importance of the number of single-photons in a data set was investigated to determine a suitable value. A reasonable idea of how many data points was needed was obtained from Moses [45]. The value 200 000 was chosen on the basis of Figure 3.9 and similar plots. If a lower value had been chosen, the accuracy of the results would decrease. The uncertainties of the resulting decay times would also be larger. If a larger value had been chosen, little would have been gained in terms of accuracy and uncertainty. The data acquisition time would have increased.

Data Collection Rate

A data acquisition rate of 1.0 photon per trigger was chosen for all the decay time measurements. The rate needs to be kept low enough so that the ADC, with a large probability, is able to distinguish all of the single-photons incident on the measuring-PMT. If the rate is too high, the results will be biased because the equipment cannot distinguish all the single-photons. On the other hand, a low rate causes a longer data acquisition time. The rate of 1.0 photon per trigger has been chosen as a value in-between these extremes. Also, since the rate influences the calculated decay time, it has been important to keep it constant. Although it is not possible to ensure the exact same rate throughout all the measurements, it has been kept constant within $\pm$ 5%.

Parameters for the Exponential Fitting

Due to the bi-exponential decay of the BGO crystals, the start point for the exponential fitting of the main decay was moved to 100 ns. This way, the upper part of the pulse was avoided. Theoretically speaking, the fast component with a decay time of 60 ns will not be gone until 300 ns have passed. This overlaps the start point for the exponential fitting of the slow component at 100 ns. After 100 ns, the fast component will have been reduced to $e^{-5/3}$, or about 19%, of its maximum amplitude. Considering the fact that it contains only 10% of the total amount of scintillation light in the pulse, its magnitude is insignificant after 100 ns. Starting the exponential fitting of the main decay component after 100 ns is therefore not a problem.

For BGO, an end point of 600 ns was used for the exponential fitting. The importance of this value is more to have a common value for comparison of all the measurements than what the exact value actually is.

For the LYSO crystals, the start point for the exponential fitting was chosen as the bin with the maximum number of counts. Since the scintillation pulse of the LYSO crystals show only single-exponential behavior, the exact start point is of less significance.

The decay time of the LYSO crystals is calculated with 160 ns as the end point for the exponential fitting. As shown in Figure 3.11, the calculated decay time varies significantly with varying end point. An exponentially decaying pulse is gone after five decay times. The fact that 160 ns is in the order of 3 decay times for an LYSO crystal was kept in mind when choosing the end point, but the exact value is chosen more or less arbitrarily. The main point has not been the exact value, but rather to have one specific end point to be able to compare the different decay times.

Black Box

The black box was found to not be sufficiently light proof. Light leakage is especially visible on the measurements of decay time. Since the arrival times of leakage photons is randomly distributed, they appear as a raising of the baseline in the pulse shape histogram. This is how the light leakage was initially discovered. The results presented here have been analyzed on data measured after additional light proofing of the box, as described in Section 2.1.1.

Teflon Tape

The crystals have been wrapped in teflon tape. This has been done to avoid that a large fraction of the scintillation light escapes the crystal without being detected. The thickness of the teflon tape layer varies on the different crystals. This results in more light loss from crystals with a thinner layer. This will in turn influence the number of scintillation photons incident on the photodetector, and hence the energy resolution. The influence of these differences is not fully controlled, but the crystals are wrapped in approximately the same number of layers of teflon tape. It is therefore reasonable to believe that the influence of the varying teflon layer is less significant than the variations in different crystals.

The use of teflon tape also influences the calculated decay time of the crystals. This is because more teflon tape increases the amount of reflections of the scintillation photons. The single-photons will then, on average, travel a longer distance before they are detected by the measuring-PMT. This will increase the calculated decay time. In a real system, these single-photons are not measured, and the decay time comes from the same pulse as the triggering-PMT is measuring in this work. This may cause a deviation of the calculated decay time using the method presented here, and the decay time in a real system. The increased decay time caused by a few layers of teflon tape is presumably in the range of a couple of nanoseconds. This would have been investigated had it not been for the fact that the measuring-PMT stopped working, and no extra PMT was available.

A possible way to examine the influence of the difference in wrapping would be to do several measurements on the same crystal, re-wrapping it between each measurement. When teflon tape, or other coating materials, are used in a real system, the crystals are only wrapped once, and then placed in the system. The re-wrapping approach has therefore not been investigated.

Chapter 5

Conclusion and Outlook

In this work, BGO and LYSO crystals of various sizes have been characterized with respect to decay time and energy resolution. The decay time of LYSO crystals is a factor six shorter than for the BGO crystals, making them far more interesting for PET applications in general, and TOF PET in particular.

The energy resolution of LYSO crystals is superior to that of BGO crystals. This was true also when optical coupling was applied. Optical coupling typically reduced the energy resolution by about one percentage point for LYSO crystals, and a few percentage points for BGO crystals.

Two radioactive sources were used to investigate the linearity of the energy spectra. For BGO, the spectrum is linear within 1% and for LYSO the spectrum is linear within 2%.

A qualitative investigation of the influence of crystal size on the interaction efficiency has been done. The area of the photopeak of the energy spectrum was compared to the total area of the spectrum. The interaction efficiency did not increase with crystal length. It did increase significantly with increasing thickness of the crystal.

For future work, it would be interesting to find the light output of the different crystals. Furthermore, testing different crystal materials such as the $LaBr_3$ would be interesting. $LaBr_3$ shows excellent energy resolution and light output, and is very fast. The downsides are its low density and the technical challenges of working with hygroscopic crystals.

Testing the crystals coupled to MPPCs must be done, as the final goal of the overall project is to build a prototype PET scanner using MPPCs instead of PMTs. This will allow for prototyping a system that is less in-

fluenced by magnetic fields, which would be necessary e.g. in combined PET/MRI (Magnetic Resonance Imaging) systems. Evaluation of a suitable fixation system is planned in the near future, making the coupling of the MPPC to the crystals more straightforward.

Simulation of the detector setup is considered for future work. Simulations will be performed using the GEANT4 toolkit. The simulations will include finding how different crystal geometries give different output signals, and how this influences parameters such as time resolution and energy resolution. The goal would be to find an optimal crystal size with respect to timing, stopping power and energy resolution. A simulation of single detectors can be used as a module in a simulation of a complete PET setup.

Bibliography

[1] Burcham WE, Jobes M. *Nuclear and Particle Physics*. Longman Scientific and Technical. 1995.

[2] Thorsteinsen TF. Kompendium i Strålingsfysikk. Fysisk institutt – Universitetet i Bergen. 1995.

[3] Johansen GA, Jackson P. *Radioisotope Gauges for Industrial Process Measurements*. John Wiley & Sons, Ltd., New York. 2004.

[4] Valk PE, Bailey DL, Townsend DW, Maisey MN. *Positron Emission Tomography: Basic Science and Clinical Practice*. Springer, 3rd edition. 2003.

[5] Cherry SR. The 2006 Henry N. Wagner Lecture: Of Mice and Men (and Positrons)—Advances in PET Imaging Technology. *J Nucl Med*. 2006; 47: 1735–45.

[6] Townsend DW. Physical principles and technology of clinical PET imaging. *Ann Acad Med Singapore*. 2004; 33: 133–45.

[7] NCRI PET Research Network. "About PET". 5 May 2010. Web. http://www.ncri-pet.org.uk/.

[8] Levin CS, Hoffman EJ. Calculation of positron range and its effect on the fundamental limit of positron emission tomography system spatial resolution. *Phys Med Biol*. 1999; 44: 781–99.

[9] Budinger TF. PET instrumentation: What are the limits? *Semin Nucl Med*. 1998; 28: 247–67.

[10] Shibuya K, Yoshida E, Nishikido F, Suzuki T, Tsuda T, Inadama N, Yamaya T, Murayama H. *Limit of Spatial Resolution in FDG-PET due*

to Annihilation Photon Non-Collinearity, volume 14 of *IFMBE Proceedings*, chapter 11, pp. 1667–71. Springer Berlin Heidelberg. 2007; .

[11] Conti M. State of the art and challenges of time-of-flight PET. *Phys Med*. 2009; 25: 1–11.

[12] van Eijk CWE. Inorganic scintillators in medical imaging. *Phys Med Biol*. 2002; 47: R85–R106.

[13] Surti S, Karp J, Muehllehner G, Raby P. Investigation of Lanthanum scintillators for 3-D PET. *IEEE Trans Nucl Sci*. 2003; 50: 348–54.

[14] Muehllehner G, Karp JS. Positron emission tomography. *Phys Med Biol*. 2006; 51: R117–R137.

[15] Surti S, Kuhn A, Werner ME, Perkins AE, Kolthammer J, Karp JS. Performance of Philips Gemini TF PET/CT Scanner with Special Consideration for Its Time-of-Flight Imaging Capabilities. *J Nucl Med*. 2007; 48: 471–80.

[16] Karp JS, Surti S, Daube-Witherspoon ME, Muehllehner G. Benefit of Time-of-Flight in PET: Experimental and Clinical Results. *J Nucl Med*. 2008; 49: 462–70.

[17] Surti S, Karp S, Popescu L, Daube-Witherspoon E, Werner M. Investigation of time-of-flight benefit for fully 3-D PET. *IEEE Trans Med Imag*. 2006; 25: 529–38.

[18] Schmitz R, Kinahan P, Harrison R, Stearns C, Lewellen T. Simulation of countrate performance for a PET scanner with different degrees of partial collimation. In *Nuclear Science Symposium Conference Record, 2005 IEEE*, volume 5. 2005; pp. 2506–9.

[19] Birks JB. *The Theory and Practice of Scintillation Counting*. Pergamon Press Ltd., Oxford. 1964.

[20] Knoll GF. *Radiation Detection and Measurement*. John Wiley & Sons, New York, 3rd edition. 2000.

[21] Krämer KW, Dorenbos P, Güdel HU, van Eijk CWE. Development and characterization of highly efficient new cerium doped rare earth halide scintillator materials. *J Mater Chem*. 2006; 16: 2773–80.

[22] Moszynski M, Kapusta M, Wolski D, Szawlowski M, Klamra W. Energy resolution of scintillation detectors readout with large area avalanche photodiodes and photomultipliers. *IEEE Trans Nucl Sci*. 1998; 45: 472–7.

[23] Saha GB. *Basics of PET Imaging – Physics, Chemistry, and Regulations*. Springer Science+Business Media, Inc., New York. 2005.

[24] Derenzo SE, Weber MJ, Bourret-Courchesne E, Klintenberg MK. The quest for the ideal inorganic scintillator. *Nucl Instrum Methods Phys Res A*. 2003; 505: 111–7.

[25] Dorenbos P. Light output and energy resolution of Ce^{3+}-doped scintillators. *Nucl Instrum Methods Phys Res A*. 2002; 486: 208–13.

[26] Moses WW. Current trends in scintillator detectors and materials. *Nucl Instrum Methods Phys Res A*. 2002; 487: 123–8.

[27] Mengesha W, Taulbee T, Rooney B, Valentine J. Light yield nonproportionality of CsI(Tl), CsI(Na), and YAP. *IEEE Trans Nucl Sci*. 1998; 45: 456–61.

[28] Dorenbos P, de Haas J, van Eijk C. Non-proportionality in the scintillation response and the energy resolution obtainable with scintillation crystals. *IEEE Trans Nucl Sci*. 1995; 42: 2190–202.

[29] Kuntner C, Aiginger H, Auffray E, Glodo J, Kapusta M, Lecoq P, Moszynski M, Schneegans M, Szupryczynski P, Wojtowicz AJ. Scintillation properties and mechanism in $Lu_{0.8}Y_{0.2}AlO_3$:Ce. *Nucl Instrum Methods Phys Res A*. 2002; 486: 176–80.

[30] Melcher CL, Schweitzer JS. A promising new scintillator: cerium-doped lutetium oxyorthosilicate. *Nucl Instrum Methods Phys Res A*. 1992; 314: 212–4.

[31] Pepin C, Berard P, Perrot AL, Pepin C, Houde D, Lecomte R, Melcher C, Dautet H. Properties of LYSO and recent LSO scintillators for phoswich PET detectors. *IEEE Trans Nucl Sci*. 2004; 51: 789–95.

[32] Moszynski M, Gresset C, Vacher J, Odru R. Timing properties of BGO scintillator. *Nucl Instrum Methods*. 1981; 188: 403–9.

[33] Qin L, Li H, Lu S, Ding D, Ren G. Growth and characteristics of LYSO ($Lu_{2(1-x-y)}Y_{2x}SiO_5$:Ce_y) scintillation crystals. *J Cryst Growth*. 2005; 281: 518–24.

[34] Ludziejewski T, Moszynska K, Moszynski M, Wolski D, Klamra W, Norlin L, Devitsin E, Kozlov V. Advantages and limitations of LSO scintillator in nuclear physics experiments. *IEEE Trans Nucl Sci*. 1995; 42: 328–36.

[35] Dorenbos P, de Haas J, van Eijk C, Melcher C, Schweitzer J. Nonlinear response in the scintillation yield of Lu_2SiO_5:Ce^{3+}. *IEEE Trans Nucl Sci*. 1994; 41: 735–7.

[36] van Loef EVD, Dorenbos P, van Eijk CWE, Krämer KW, Güdel HU. Scintillation properties of $LaBr_3$:Ce^{3+} crystals: fast, efficient and high-energy-resolution scintillators. *Nucl Instrum Methods Phys Res A*. 2002; 486: 254–8.

[37] Hamamatsu. *Handbook: Photomultiplier Tubes – Basics and Applications*. Hamamatsu Photonics K.K., Electron Tube Division, 3rd edition. 2007.

[38] Hamamatsu. *Catalog: Photomultiplier Tube Modules*. Hamamatsu Photonics K.K., Electron Tube Division. 2008. Web. 27 Apr. 2010.

[39] Hamamatsu Corporation. "Photomultiplier Tubes (PMTs)". *Hamamatsu*. Web. 30 Apr. 2010. http://sales.hamamatsu.com/en/products/electron-tube-division/detectors/photomultiplier-tubes.php.

[40] Otte N. The Silicon Photomultiplier: A New Device for High Energy Physics, Astroparticle Physics, Industrial and Medical Applications. 2006. In the Proceedings of International Symposium on Detector Development for Particle, Astroparticle and Synchrotron Radiation Experiments (SNIC 2006), Menlo Park, California, 3-6 Apr 2006.

[41] Erdal HA. Characterization of Multipixel Avalanche Photodiodes. Master's thesis, Department of Physics and Technology, University of Bergen. 2009.

[42] Brun R, Rademakers F. ROOT – An object oriented data analysis framework. *Nucl Instrum Methods Phys Res A*. 1997; 389: 81–6. See also http://root.cern.ch.

[43] Williams T, Kelley C. *Online manual: gnuplot 4.4 – An Interactive Plotting Program.* 2010. See also http://www.gnuplot.info.

[44] Bollinger LM, Thomas GE. Measurement of the Time Dependence of Scintillation Intensity by a Delayed-Coincidence Method. *Rev Sci Instrum*. 1961; 32: 1044–50.

[45] Moses WW. A method to increase optical timing spectra measurement rates using a multi-hit TDC. *Nucl Instrum Methods Phys Res A*. 1993; 336: 253–61.

Appendices

Appendix A

Data Sheets of Scintillator Crystals

Included below are data sheets of the scintillator crystals used in this work. The only data sheets available from ScintiStone on their crystals is their web page information. Due to the limited amount of information therein, the data sheets from Saint Gobain has also been included for the LYSO crystals.

ScintiStone Technology

More photons for less!

BGO

< Return to Product List

Price: Get a quote.

Product Summary

Bismuth germanate ($Bi_4Ge_3O_{12}$), commonly abbreviated as BGO, is the crystalline form of an inorganic oxide with cubic eulytine structure, which is colorless, transparent and insoluble in water. When exposed to the irradiation of high energy particles or other sources, such as gamma-rays or X-rays, it emits green fluorescent light with a peak wavelength of 480nm. Because of its high stopping power, high scintillation efficiency, good energy resolution and non-hygroscopic, BGO has been found a wide range of applications in high energy physics, nuclear physics, space physics, nuclear medicine, geological exploration and other industries.

Physical properties of BGO crystal

Density (g/cm^3)	7.13
Radiation length (cm)	1.12
Decay constant (μs)	0.3
Wavelength of max emission	480
Light yield (%NaI:Tl)	8
Melting point (C)	1050
Hardness (Mho)	5
Refractive index	2.15
Hygroscopicity	None
Cleavage	None

ScintiStone Technology

More photons for less!

LYSO/LSO

< Return to Product List

Price: Get a quote.

Product Summary

LYSO (Cerium-doped Lutetium Yttrium Orthosilicate.) LYSO crystal has the advantages of high light output and density, quick decay time, excellent energy resolution and low cost. These properties make LYSO an ideal candidate for a range of ray detection applications in nuclear physics and nuclear medicine, which require higher, improved timing resolution and superior energy revolution.

We can provide LYSO in any volumes requested and can also supply customized pixel arrays or module configurations.

Physical properties of LYSO crystal

Density (g/cm^3)	7.3
Radiation length (cm)	1.16
Decay constant (ns)	50
Wavelength of max emission	420
Light yield (%NaI:Tl)	75
Melting point (C)	2047
Refractive index	1.82

Right click to open our web site in your browser:
www.detectors.saint-gobain.com

PreLude® 420

It's what's Inside that Counts!

Scintillation Material

PreLude™ 420 ($Lu_{1.8}Y_{.2}SiO_5$:Ce) is a Cerium doped lutetium based scintillation crystal that offers high density and a short decay time. It has an improved light output and energy resolution compared to BGO ($Bi_4Ge_3O_{12}$), which has a similar density. Applications that require higher throughput, better timing and better energy resolution will benefit from using PreLude 420 material.

PreLude 420 scintillator has shown up to three to four times the light emission of BGO. The measured energy resolution for 662 keV photons for a 30mm diameter x 15mm long crystal is 7.1% (see the energy spectrum below). A typical value for BGO is 12%.

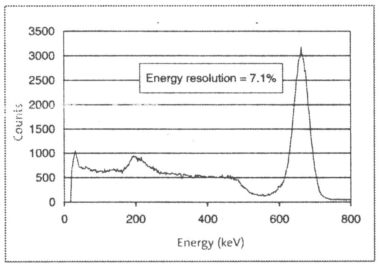

Figure 1. PreLude™ 420 Response to 662 keV Photons

The 1/e decay time of PreLude 420 crystal is 41ns, which is much shorter than the decay time of BGO. It is a single exponential with no long components present. This allows for higher rates, greater throughput and better timing.

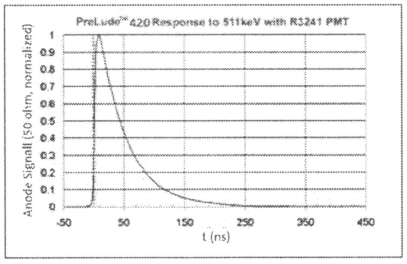

Figure 2. PreLude™ 420 response to 511 keV with R3241 PMT

The emission of scintillation light matches well with the sensitivity spectrum of most PMTs. The quantum efficiency (Q.E.) of a standard bialkali ETI 9266 PMT is 25% at the peak of the emission.

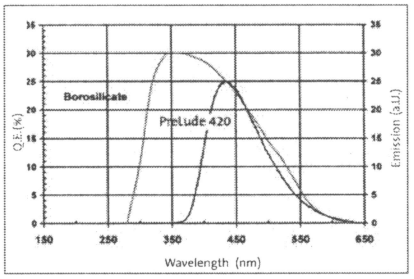

Figure 3. PreLude™ 420 Emission & ETI 9266 Q.E.
(Q.E. data courtesy of Electron Tubes, Inc.)

PET applications have traditionally used arrays of BGO. PreLude 420 crystal competes directly on density and surpasses BGO on energy resolution, timing and throughput.

The PreLude 420 material is a lutetium-based scintillator which contains a radioactive isotope ^{176}Lu, a naturally occurring beta emitter. ^{176}Lu beta decays to ^{176}Hf 99.66% of the time to the 597 keV excited state. This state decays with a 3 gamma ray cascade of 307, 202 and 88 keV. The 1" diameter by 1" long PreLude 420 crystal absorbs

continued on back..

Properties –

Density [g/cm³]: 7.1

Hygroscopic ..... no

Attenuation length for 511keV (cm): .. 1.2

Wavelength of emission max.[nm] 420

Refractive index@emission max. 1.81

Decay time [ns]: 41

Energy resolution [%]: 8.0

Light yield [photons/keVγ]: 32

Average temperature coefficient from 25 to 50° C (%/°C): ..... -0.28

Photoelectron yield [% of NaI(Tl)] (for γ-rays) 75

SAINT-GOBAIN
CRYSTALS

PreLude™420 Scintillation Material

nearly 100% of the beta particles. However, some of the photons escape leading to four sets of beta+gamma distributions. These four sets of beta distributions, based on which gamma rays are detected in coincidence, are identified in Figure 4. The total rate for this activity is 39 cps/g.

The light yield as a function of temperature was measured with ^{137}Cs excitation at two amplifier shaping times of 1µs and 12µs. The temperature of the PMT was maintained constant while the temperature of the scintillator was varied from -65°C to +175°C. Results are shown in Figure 5.

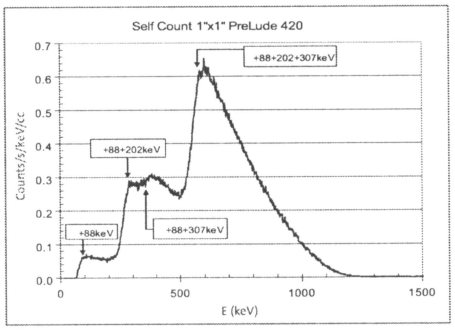

Figure 4. Beta distributions

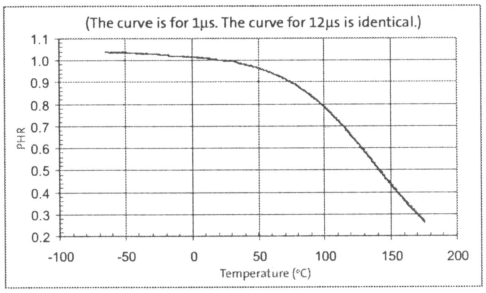

Figure 5. Temperature response

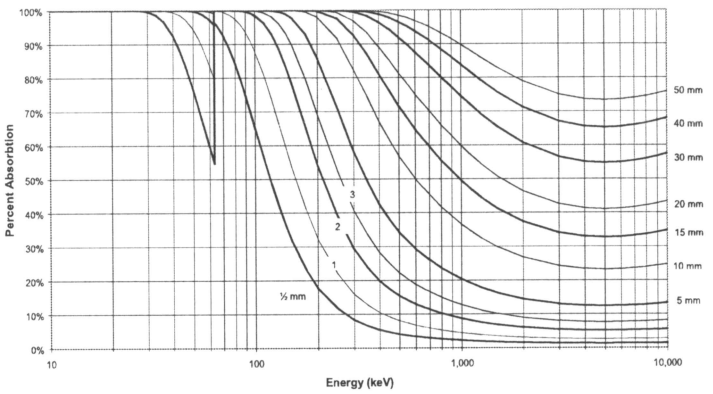

Absorption Efficiency of PreLude®420

Figure 6. Gamma and X-ray absorption efficiency for various thicknesses of PreLude 420 material. Data compiled by C. M. Rozsa (presented in Saint-Gobain Crystals brochure "Efficiency for Selected Scintillators.")

Table comparing principal properties of PreLude™420 versus BGO and LSO

Property	PreLude 420	BGO	LSO
Density [g/cm³]	7.1	7.1	7.4
Attenuation length for 511 keV (cm)	1.2	1.0	1.15
Decay time [ns]	41	300	40
Energy resolution	8.0	12.0	10.0
Light output, photons per keV	32	9	26
Average temperature coefficient 25 to 50°C (%/°C)	-0.28	-1.2	-1.3

Saint-Gobain Crystals
17900 Great Lakes Parkway
Hiram, OH 44234
Tel: (440) 834-5600
Fax: (440) 834-7680

Europe

Saint-Gobain Crystals
104 Route de Larchant
BP 521
77794 Nemours Cedex, France
Tel: 33 (1) 64 45 10 10
Fax: 33 (1) 64 45 10 01

P.O. Box 3093
3760 DB Soest
The Netherlands
Tel: 31 35 60 29 700
Fax: 31 35 60 29 214

Japan

Saint-Gobain KK, Crystals Division
3-7, Kojimachi, Chiyoda-ku,
Tokyo 102-0083 Japan
Tel: 81 (0) 3 3263 0559
Fax: 81 (0) 3 5212 2196

China

Saint-Gobain China Investment Co., Ltd.
15-01 CITIC Building
19 Jianguomenwai Ave.
Beijing 100004 China
Tel: 86 (0) 10 6513 0311
Fax: 86 (0) 10 6512 9843

www.detectors.saint-gobain.com

(07-08)

Appendix B

Data Sheets of Detector Equipment

Included below are data sheets / product specification sheets of photodetectors, the ADC, and optical greases used in the experiments.

Metal Package PMT

Photosensor Modules H5773/H5783/H6779/H6780 Series

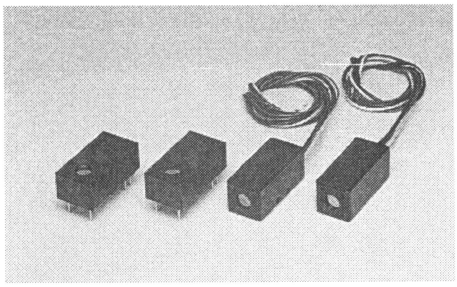

The H5773/H5783/H6779/H6780 series are photosensor modules housing a metal package PMT and high-voltage power supply circuit. The metal package PMTs have a metallic package with the same diameter as a TO-8 package used for semiconductor photodetectors, and deliver high gain, wide dynamic range and high-speed response while maintaining small dimensions identical to those of photodiodes. The internal high-voltage power supply circuit is also compact, making the module easy to use.

Considering the mounting methods, a cable output type and a pin output type are provided, and a total of 7 types are available according to the wavelength range to be measured. A P-type is also available with selected gain and dark count ideal for photon counting under extremely low light conditions.

Product Variations

Type No. \ Suffix	None	-01	-02	-03	-04	-06	-20	Output Type	Features
H5773	yes	yes	yes	yes	yes	yes	yes	On-board	Low power consumption
H5783	yes	yes	yes	yes	yes	yes	yes	Cable output	
H5773P	yes	no	no	no	no	no	no	On-board	For photon counting
H5783P	yes	no	no	no	no	no	no	Cable output	Low power consumption
H6779	yes	yes	yes	yes	yes	yes	yes	On-board	Low ripple noise
H6780	yes	yes	yes	yes	yes	yes	yes	Cable output	Fast settling time

Suffix	Spectral Response
None	300 nm to 650 nm
-01	300 nm to 850 nm
-02	300 nm to 880 nm
-03	185 nm to 650 nm
-04	185 nm to 850 nm
-06	185 nm to 650 nm
-20	300 nm to 900 nm

The suffix -06 type (synthetic silica window) has higher sensitivity than the -03 type below 300 nm in wavelength range.

Specifications

Parameter			H5773 / H5783 / H6779 / H6780 Series					Unit
Suffix			None	-03, -06	-01, -04	-02	-20	—
Input Voltage			+11.5 to +15.5					V
Max. Input Voltage			+18					V
Max. Input Current			H5773 / H5783 Series: 9 H6779 / H6780 Series: 30					mA
Max. Output Signal Current			100					μA
Max. Control Voltage			+1.0 (Input impedance 100 kΩ)					V
Recommended Control Voltage Adjustment Range			+0.25 to +0.9					V
Effective Area			φ8					mm
Sensitivity Adjustment Range			1: 10^4					—
Peak Sensitivity Wavelength			420	420	400	500	630	nm
Cathode	Luminous Sensitivity	Min.	40	40	80	200	350	μA/lm
		Typ.	70	70	150	250	500	
	Blue Sensitivity Index (CS 5-58)		8	8	—	—	—	—
	Red/White Ratio		—	—	0.2	0.25	0.45	—
	Radiant Sensitivity *1		62	62	60	58	78	mA/W
Anode Standard Type	Luminous Sensitivity	Min.	10	10	15	25	35	A/lm
		Typ.	50	50	75	125	250	
	Radiant Sensitivity *1 *2		4.3×10^4	4.3×10^4	3.0×10^4	2.9×10^4	3.9×10^4	A/W
	Dark Current *2 *3	Typ.	0.2	0.2	0.4	2	2	nA
		Max.	2	2	4	20	20	
Anode P Type	Gain *2	Min.	7.5×10^5	—				—
		Typ.	1×10^6	—				
	Radiant Sensitivity *1 *2		6.2×10^4	—				A/W
	Dark Count *2 *3	Typ.	80	—				s^{-1}
		Max.	400	—				
Rise Time *2			0.78					ns
			H5773 Series	H5783 Series	H6779 Series	H6780 Series		
Ripple Noise *2 *4 (peak to peak)		Max.	1.2		0.6			mV
Settling Time *5			2		0.2			s
Operating Ambient Temperature			+5 to +50		+5 to +45			°C
Storage Temperature			-20 to +50					°C
Weight			60	80	60	80		g

*1: Measured at the peak sensitivity wavelength *2: Control voltage = +0.8 V *3: After 30 minute storage in darkness
*4: Cable RG-174/U, Cable length 450 mm, Load resistance = 1 MΩ, Load capacitance = 22 pF
*5: The time required for the output to reach a stable level following a change in the control voltage from +1.0 V to +0.5 V.

Characteristics (Cathode radiant sensitivity, Gain)

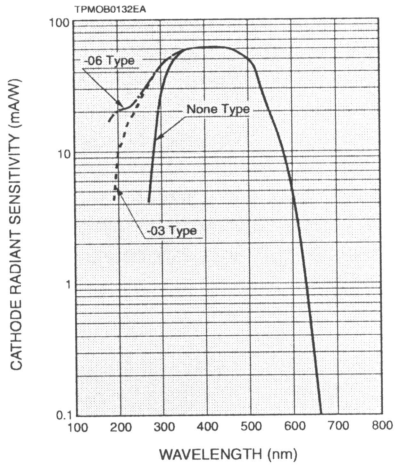

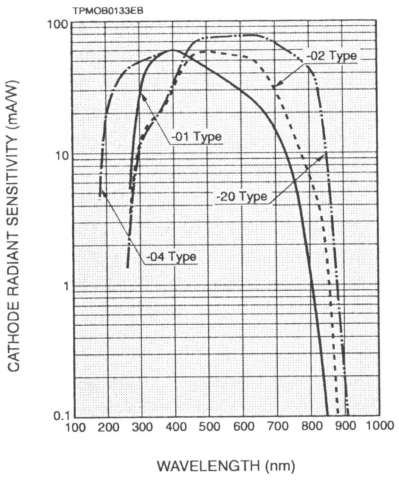

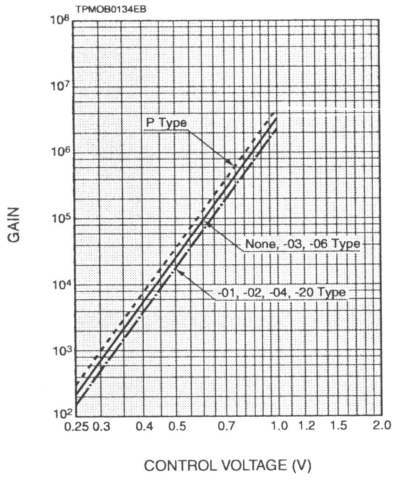

Sensitivity Adjustment Method

Voltage Programming

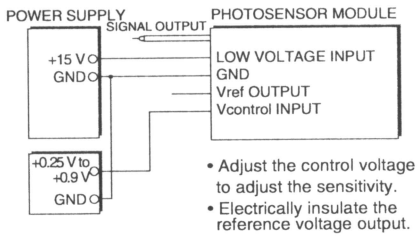

- Adjust the control voltage to adjust the sensitivity.
- Electrically insulate the reference voltage output.

Resistance Programming

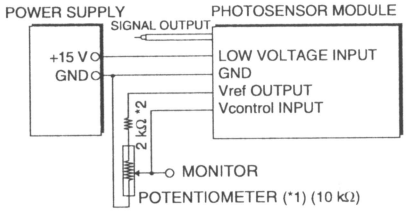

*1: When using a potentiometer to adjust sensitivity, monitor the control voltage so it does not exceed +1.0 V.

*2: H6779/H6780 series has this 2 kΩ resistor.
No external resistor is needed.

TPMOC0131EC

Dimensional Outlines (Unit: mm)

H5773/H6779 Series

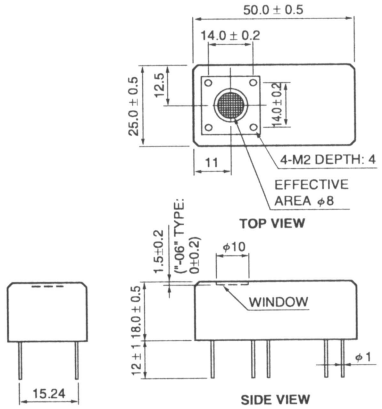

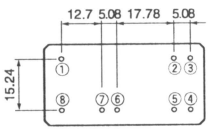

①NO CONNECTION
②Vref OUTPUT (+1.2 V)
③Vcontrol INPUT (+0.25 V to +0.9 V)
④LOW VOLTAGE INPUT (+15 V)
⑤GND
⑥SIGNAL GND
⑦SIGNAL OUTPUT
⑧NO CONNECTION

TPMOA0010EC

H5783/H6780 Series

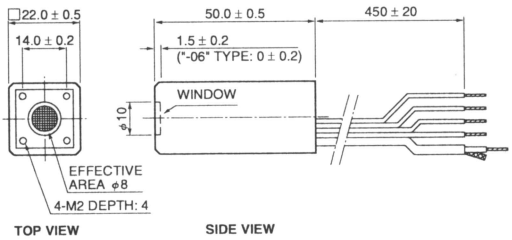

LOW VOLTAGE INPUT: AWG26 (RED, +15 V)
GND : AWG26 (BLACK)
Vref OUTPUT : AWG26 (BLUE, +1.2 V)
Vcontrol INPUT : AWG26 (WHITE, +0.25 V to +0.9 V)
SIGNAL OUTPUT : RG-174/U

TPMOA0011EC

Option (Optical Fiber Adapter) (Unit: mm)

E5776 (FC Type)

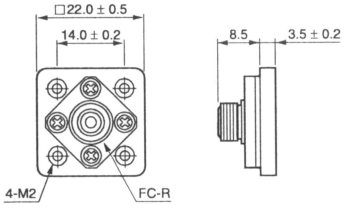

TACCA0055EA

E5776-51 (SMA Type)

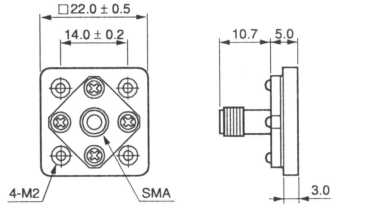

TACCA0239EA

2. Active area: 3 × 3 mm type

These MPPCs have an effective active area of 3 × 3 mm and are available in two different packages (ceramic and SMD).

- **Ceramic type**:
  S10362-33-025C, S10362-33-050C, S10362-33-100C

- **SMD type**:
  S10931-025P, S10931-050P, S10931-100P

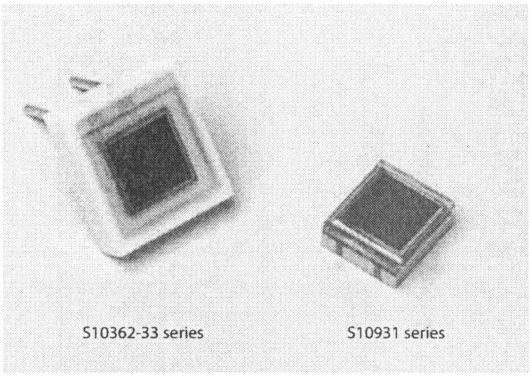

Specifications (Typ. Ta=25 °C, unless otherwise noted)

Parameter	Symbol	S10362-33 series			S10931 series			Unit
		-025C	-050C	-100C	-025P	-050P	-100P	
Effective active area	-	3 × 3			3 × 3			mm
Number of pixels	-	14400	3600	900	14400	3600	900	-
Pixel size	-	25 × 25	50 × 50	100 × 100	25 × 25	50 × 50	100 × 100	μm
Fill factor *1	-	30.8	61.5	78.5	30.8	61.5	78.5	%
Spectral response range	λ	320 to 900			320 to 900			nm
Peak sensitivity wavelength	λp	440			440			nm
Operating voltage range	-	70 ± 10 *2			70 ± 10 *2			V
Dark count *3	-	4	6	8	4	6	8	Mcps
Dark count Max. *3	-	8	10	12	8	10	12	Mcps
Terminal capacitance	Ct	320			320			pF
Time resolution (FWHM) *4	-	500 to 600			500 to 600			ps
Temperature coefficient of reverse voltage	-	56			56			mV/°C
Gain	M	2.75×10^5	7.5×10^5	2.4×10^6	2.75×10^5	7.5×10^5	2.4×10^6	-

*1: Ratio of the active area of a pixel to the entire area of the pixel
*2: For the recommended operating voltage of each product, refer to the data attached to each products.
*3: 0.5 p.e. (threshold level)
*4: Single photon level
Note: Each value was measured at recommended operating voltage (refer to the data attached to each product).
The last letter of each type number indicates package materials (C: ceramic, P: SMD).

Photon detection efficiency (PDE) vs. wavelength (typical example)

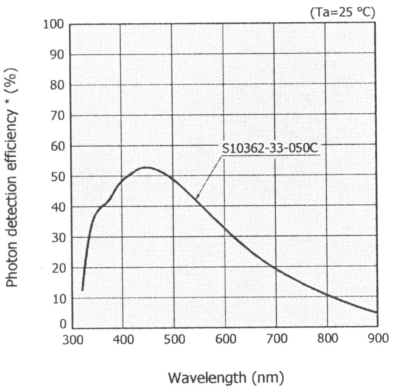

* Photon detection efficiency includes effects of crosstalk and afterpulses.

KAPDB00173EA

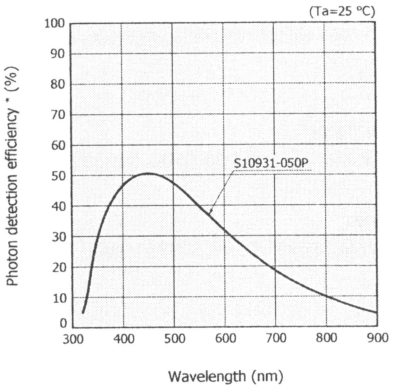

* Photon detection efficiency includes effects of crosstalk and afterpulses.

KAPDB0174EA

Dimensional outlines (unit: mm, tolerance: ±0.1 mm unless otherwise noted)

S10362-33-025C/-050C/-100C

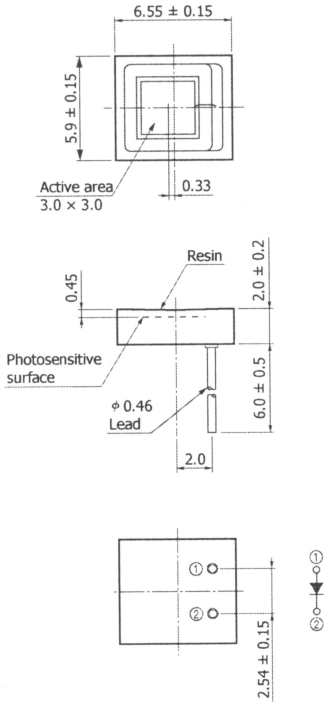

KAPDA0123EB

S10931-025P/-050P/-100P

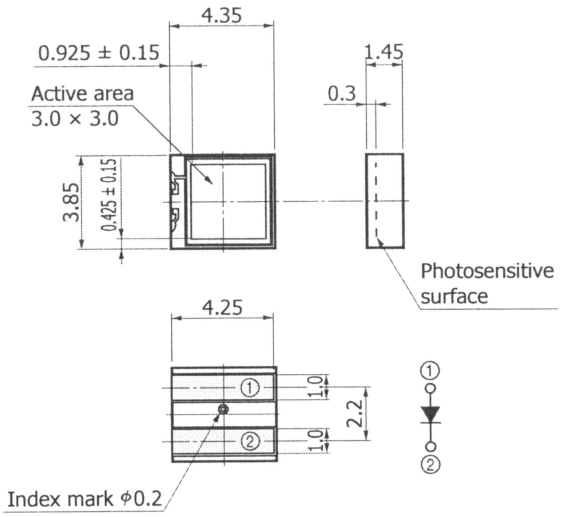

KAPDA0125EC

Electronic Instrumentation

V1729A
4 Channel 14 bit 2 GS/s (300 MHz bandwidth) Switched-Capacitor Digitizer

Technical Specifications Table	
A/D conversion	14 bit
Full scale range	±1 V
LSB	125 µV
Max Sampling frequency	2 GHz
Bandwidth	300 MHz
INL	±0.1 %
DNL	±0.05 %
Internal clock frequency	50 MHz or 100 MHz
Dead time	Adjustable from 1 to 65535 clock cycles
VME modes	A32/D64, A32/D32, A24/D16

close

Detector Assembly Materials

Assembly Materials Available –

Optical Cement

Reflector Paint for Plastic Scintillators

Reflector Paint for Liquid Scintillator Tanks

Silicone Optical Grease

Optical Interface Pads

Black Wrapping Tape

Plastic Masking Paper

PTFE Reflector Tape

Saint-Gobain Crystals can provide you with various detector assembly materials. For more detailed specifications on BC-600, BC-620 and BC-622A, individual data sheets are available.

BC-600 Optical Cement –

BC-600 optical cement is a clear epoxy, which sets at room temperature and has a refractive index close to that of SGCD plastic scintillators. It is therefore ideal for optically cementing plastic scintillators to light pipes or optical windows. It is not recommended for coupling scintillators to photomultiplier tubes. For that application, we recommend BC-634A or BC-630.

BC-620 Reflector Paint for Plastic Scintillators –

BC-620 is a highly efficient reflector employing a special grade of titanium dioxide in a water soluble binder. It is applied directly onto plastic scintilllators, acrylic light guides, glass and metals. It is not intended for direct contact with liquid scintillators. It is a diffuse reflector and, therefore, should not be applied to sheets of scintillator or light guide material where the length is much longer than the thickness

BC-622A Reflector Paint for Liquid Scintillator Tanks –

BC-622A reflector paint is intended for use with liquid scintillators. It is particularly useful in large steel or aluminum tanks, which require application of the apint at the research site. It is a diffuse reflector and, therefore, should not be used on the major surfaces of long, narrow tanks (total internal reflector and employed in these).

BC-630 Silicone Optical Grease –

BC-630 is a clear, colorless, silicone, optical coupling compound that features excellent light transmission and low evaporation and bleed at 25°C. It has a specific gravity of 1.06 and an Index of Refraction of 1.465. We supply this single component formulation in 60ml (2oz.) jars.

BC-634A Optical Interface Pad –

It is formulated for use within the temperature range of -10 to +60°C.

BC-637 High Temperature Optical Interface Pad –

BC-637 interface pads are placed between the plastic and photomultiplier tube. BC-637 is rated at 200°C.

CARGILLE

May 15, 2004

OPTICAL GEL CODE 0608

n (5893 Å) 25 °C = 1.457

TYPICAL CHARACTERISTICS

COMPOSITION	Aliphatic Hydrocarbons & Gelling Agents
APPEARANCE	Colorless Gel
ODOR	None
COLOR STABILITY	In sun: no visible change after 9 years
INDEX CHANGE RATE BY EVAPORATION	Very low: 0.0000 expected:

exposed surface area to volume ratio of 0.2 sq. cm / cc @ 25 °C for 32 days

FREEZING POINT °C	-67
BOILING POINT °C @ 760mm Hg	> 416
FLASH POINT °C COC	> 245
DENSITY g / cc @ 25 °C	0.878
DENSITY TEMP. COEF. g / cc / °C	-0.0007
COEF. OF THERM. EXP. cc / cc °C	0.0008
VISCOSITY @ 25 °C	Soft Gel
OIL SEPARATION 100 °C for 24 Hours, % by Weight	< 0.05
WEIGHT LOSS 100 °C for 24 Hours, %	< 0.05
WATER IMMERSION	No Effect

PARTLY SOLUBLE: Carbon Tetrachloride, Ethyl Ether, Freon TF, Heptane, Methylene Chloride, Naphtha, Toluene, Turpentine, Xylene

INSOLUBLE: Acetone, Ethanol, Water CLEAN UP; Wipe surfaces clean, then use soap and water.

COMPATIBLE 10 month immersion @ 25 °C: Acrylic, Cellulose Acetate, Epoxy, Mylar, Nylon, Polycarbonate, Polyester, Polyethylene, Polypropylene, Polystyrene, Polyurethane, Polyvinyl Chloride, Phenolic, Teflon; Silicone and Fluorosilicone Rubber; Neoprene Rubber, Aluminum, Copper, Brass, and Steel; (tests done on one example of each)

INCOMPATIBLE: Latex Rubber, Tygon (types: S-50-HL, R-3603, B-44-3)

TOXICITY ..... Low (request MSDS)

CAUCHY EQUATION: refractive index as a function of wavelength at 25 °C

W = wavelength in angstroms (Å)

$n(W) = 1.44514 + (431760) / W^2 + (-1.80659E+11) / W^4$

SOURCE OR SPECTRAL LINE	WAVELENGTH (angstroms)	REFRACTIVE INDEX 25 °C	% TRANSMITTANCE 25 °C 1mm	1 cm	10cm
near UV cut off	3200	1.486	70	3	0
i (Hg)	3650	1.477	98	84	16
h (Hg)	4047	1.471	99	91	40
F**?** (Cd)	4800	1.464	100	97	71
F (H)	4861	1.463	100	97	72
e (Hg)	5461	1.459	100	98	80
D (Na D1, D2 mean)	5893	1.457	100	99	90
HeNe laser	6328	1.456	100	99	92
C? (Cd)	6439	1.455	100	100	95
C (H)	6563	1.455	100	100	96
Ruby Laser	6943	1.454	100	100	99
GaAs laser	8400	1.451	100	100	99
Nd: YAG laser	10648	1.449	100	97	74
Diode	13000	1.448	99	91	39
Diode	15500	1.447	98	83	16

$n_F - n_C$	=	0.008
Abbe ν_D : $(n_D-1) / (n_F-n_C)$	=	57
Temp. Coef: dn_D / dt 15-35 °C	=	-0.00035

CARGILLE LABORATORIES INC.

55 Commerce Road, Cedar Grove, NJ 07009-1289 U.S.A.

Phone: 973-239-6633 / Fax: 973-239-6096 / URL : www.cargille.com

Appendix C

Data Sheets of Radioactive Sources

Below are included data sheets of the radioactive sources used during this work.

RADIONUCLIDE SAFETY DATA SHEET

NUCLIDE: Cs-137 **FORMS: ALL SOLUBLE**

PHYSICAL CHARACTERISTICS:

HALF-LIFE: 30.17 years

TYPE DECAY: Beta/Gamma
Maximum betas energy 0.512MeV
1.176 MeV (7 %)
gamma: 0.662 MeV (85 %)

Hazard category: C- level (low hazard) 10 uCi to 2000 uCi
B - level (Moderate hazard) : > 2001- 100,000 uCi
A - level (High hazard) : > 100,000 uCi

EXTERNAL RADIATION HAZARDS AND SHIELDING:

The maximum range of the beta ~490 cm in air, and 0.53 cm in lucite.
The gamma exposure rate at 1 cm from 1 mCi is 3400 mR/hr. The exposure rate varies directly with activity and inversely as the square of the distance. The tenth value layer of lead is 2.1 cm.

HAZARDS IF INTERNALLY DEPOSITED:

Cs137 has a biological half-life of 70 days, and an effective half- life of 70 days
The Minium Ingestion ALI: 100uCi equals 5 rem TEDE (Whole Body)
The Minium Inhalation ALI: 200 uCi equals 5 rem TEDE (Whole Body
The Critical Organ is the whole body.

DOSIMETRY AND BIOASSAY REQUIREMENTS:

Film badges and dosimeter rings are required if 5 millicuries are handled at any one time or millicurie levels are handled on a frequent (daily) basis.

Urine assays may be required after spills or contamination incidents.

SPECIAL PROBLEMS AND PRECAUTIONS:

1. Work behind shielding consisting of lucite (inner) and lead (out). Handle stock solution vials in shields or use tongs or forceps. Change gloves often.

2. Segregate wastes to those with half-lives greater than 90 days (but not with H3 and/or C14).

3. Limit of soluble waste to sewer 10 microcuries/ day per lab.

9/03

RADIONUCLIDE SAFETY DATA SHEET

NUCLIDE: Na-22 **FORMS: ALL SOLUBLE**

PHYSICAL CHARACTERISTICS:

HALF-LIFE: 2.6 years
TYPE DECAY: positron emission --- maximum energy 0.545 MeV
gamma ray associated with annihilation 0.511 MeV
accompanying gamma photons 1.275 MeV

Hazard category: C- level (low hazard) : 0.001 to 0.1 mCi
B - level (Moderate hazard) : > 0.1 mCi to 10 mCi
A - level (High hazard) : greater than 10 mCi

EXTERNAL RADIATION HAZARDS AND SHIELDING:

The gamma exposure rate at 1 cm from 1 mCi of Na22 shielded for positrons is 12000 mR/hr. The half and tenth values of lead for this gamma are 0.9 and 3.6 cm respectively. The maximum exposure rate at 1 foot from such storage areas must be shielded to less than 2 mR/hr.

The dose rate from the positrons is 310,000 mrads/hr at 1 cm per mCi. The maximum range of the positrons is about 44 inches in air, and about 0.06 inches in lucite. The use of the lead shield for storage will provide and adequate shield for the positron particles.

HAZARDS IF INTERNALLY DEPOSITED:

It is important to avoid ingestion and /or skin contamination.

The Annual Limit of Intake based on a whole body dose of 500 mrem per year is 54 microcuries. The maximum permissible body burden is 10 microcuries; the critical organ being the body fluids.

DOSIMETRY AND BIOASSAY REQUIREMENTS:

Film badges and dosimeter rings are required if 0.5 millicuries or more are being handled at any one time or 0.1 millicurie levels are handled on a frequent (daily) basis.

SPECIAL PROBLEMS AND PRECAUTIONS:

1. Work behind shielding, preferably transparent materials. Use remote handling whenever possible.

2. Survey frequently. Change gloves often.

3. Segregate wastes to those with half-lives greater than 90 days (but not with H3 and/or C14).

4. Limit of soluble waste to sewer: 1 microcurie per day per lab.